Journal of Hazardous Materials 435 (2022) 129053

Contents lists available at ScienceDirect

Journal of Hazardous Materials

journal homepage: www.elsevier.com/locate/jhazmat

Research Paper

Hazard assessment of abraded thermoplastic composites reinforced with reduced graphene oxide

Savvina Chortarea [a], Ogul Can Kuru [a], Woranan Netkueakul [a], Marco Pelin [b], Sandeep Keshavan [c], Zhengmei Song [d], Baojin Ma [d], Julio Gómes [e], Elvira Villaro Abalos [f], Luis Augusto Visani de Luna [g,h,i], Thomas Loret [g,h,i], Alexander Fordham [g,h,i], Matthew Drummond [g,h], Nikolaos Kontis [j], George Anagnostopoulos [j], George Paterakis [j], Pietro Cataldi [h,l], Aurelia Tubaro [b], Costas Galiotis [j,k], Ian Kinloch [h,l], Bengt Fadeel [c], Cyrill Bussy [g,h,i], Kostas Kostarelos [g,h,m], Tina Buerki-Thurnherr [a], Maurizio Prato [n,o,p], Alberto Bianco [d], Peter Wick [a,*]

[a] Swiss Federal Laboratories for Materials Science and Technology (Empa), Laboratory for Particles-Biology Interactions, 9014 St. Gallen, Switzerland
[b] Department of Life Sciences, University of Trieste, 34127 Trieste, Italy
[c] Nanosafety & Nanomedicine Laboratory, Institute of Environmental Medicine, Karolinska Institutet, 177 77 Stockholm, Sweden
[d] CNRS, Immunology, Immunopathology and Therapeutic Chemistry, UPR3572, University of Strasbourg, ISIS, 67000 Strasbourg, France
[e] Avanzare Innovacion Tecnologica S.L. 26370 Navarrete, Spain
[f] Instituto de Tecnologías Químicas de La Rioja (InterQuímica), 26370 Navarrete, Spain
[g] Nanomedicine Lab, Faculty of Biology, Medicine & Health, University of Manchester, Manchester M13 9PT, United Kingdom
[h] National Graphene Institute, University of Manchester, Manchester M13 9PL, United Kingdom
[i] Lydia Becker Institute of Immunology and Inflammation, Faculty of Biology, Medicine and Health, University of Manchester, Manchester Academic Health Science Centre, Manchester M13 9PL, United Kingdom
[j] Institute of Chemical Engineering Sciences, Foundation of Research and Technology-Hellas (FORTH/ICE-HT), 26504 Patras, Greece
[k] Department of Chemical Engineering, University of Patras, 26504 Patras, Greece
[l] Department of Materials, University of Manchester, Manchester M13 9PL, United Kingdom
[m] Catalan Institute of Nanoscience and Nanotechnology (ICN2), and Barcelona Institute of Science and Technology (BIST), Barcelona 08193, Spain
[n] Department of Chemical and Pharmaceutical Sciences, University of Trieste, 34127 Trieste, Italy
[o] Center for Cooperative Research in Biomaterials (CIC biomaGUNE), Basque Research and Technology Alliance (BRTA), 20014 Donostia San Sebastián, Spain
[p] Basque Foundation for Science (IKERBASQUE), 48013 Bilbao, Spain

HIGHLIGHTS

- Graphene related materials are extensively used to reinforce polymers.
- Abrasion of composite materials is an important end-of-life scenario to be assessed prior to their commercial use.
- This study provides a qualitative and quantitative analysis of the released materials after abrasion.
- The hazard of abraded thermoplastics is assessed focusing on the most likely exposure routes.
- Life cycle considerations and impact of reduced graphene oxide in the context of reinforced polymers are addressed.

GRAPHICAL ABSTRACT

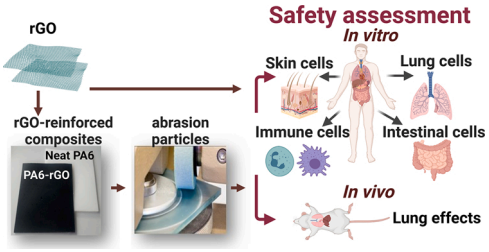

Abbreviations: GRM, graphene related materials; PA6, Polyamide 6; rGO, reduced graphene oxide.

* Correspondence to: Swiss Laboratories for Materials Science and Technology, Lerchenfeldstrasse 5, CH-9014 St. Gallen, Switzerland.
E-mail address: peter.wick@empa.ch (P. Wick).

https://doi.org/10.1016/j.jhazmat.2022.129053
Received 13 February 2022; Received in revised form 22 April 2022; Accepted 29 April 2022
Available online 5 May 2022

ARTICLE INFO

Editor: Dr. S Nan

Keywords:
Graphene-related materials
Thermoplastic polymer composites
Hazard assessment

ABSTRACT

Graphene-related materials (GRMs) are subject to intensive investigations and considerable progress has been made in recent years in terms of safety assessment. However, limited information is available concerning the hazard potential of GRM-containing products such as graphene-reinforced composites. In the present study, we conducted a comprehensive investigation of the potential biological effects of particles released through an abrasion process from reduced graphene oxide (rGO)-reinforced composites of polyamide 6 (PA6), a widely used engineered thermoplastic polymer, in comparison to as-produced rGO. First, a panel of well-established *in vitro* models, representative of the immune system and possible target organs such as the lungs, the gut, and the skin, was applied. Limited responses to PA6-rGO exposure were found in the different *in vitro* models. Only as-produced rGO induced substantial adverse effects, in particular in macrophages. Since inhalation of airborne materials is a key occupational concern, we then sought to test whether the *in vitro* responses noted for these materials would translate into adverse effects *in vivo*. To this end, the response at 1, 7 and 28 days after a single pulmonary exposure was evaluated in mice. In agreement with the *in vitro* data, PA6-rGO induced a modest and transient pulmonary inflammation, resolved by day 28. In contrast, rGO induced a longer-lasting, albeit moderate inflammation that did not lead to tissue remodeling within 28 days. Taken together, the present study suggests a negligible impact on human health under acute exposure conditions of GRM fillers such as rGO when released from composites at doses expected at the workplace.

Graphene and its derivatives (graphene-related materials or GRMs) have been among the fastest growing areas of nanoscience and technology over the past decade. This atomically thin, two-dimensional form of carbon has generated considerable excitement since its initial discovery. Due to its outstanding physicochemical properties, namely, excellent stretchability (20% of its initial length), high intrinsic mechanical stiffness and strength (1 TPa and 130 GPa, respectively), extraordinary electrical conductivity (mobility of charge carriers 200,000 cm^2/ V/s), large surface area (2630 m^2/g), and superior thermal conductivity (~5000 W/mK), it has raised high expectations on future applications (George et al., 2018; Novoselov et al., 2012; Geim and Novoselov, 2007). Many of these properties are superior to those of other materials, but most importantly, the combination of all these characteristics is exceptional. It is of no surprise that GRMs are currently being explored for a multitude of applications, such as in electronics, energy, photonics, composite, filtration, sensors, or biomedicine (Ferrari et al., 2015). As a result of the increased demand, production of GRMs has increased from 14 tons in 2009 to nearly 1200 tons per year within just a decade. By 2025, the market value is projected to reach between ~US$180 million to US$2.1 billion per year (Reiss et al., 2019; Kong et al., 2019), with about 30% of the annual growth rate for graphene reinforced composites (Reiss et al., 2019).

In this respect, GRMs have been proposed as alternative fillers (*i.e.*, materials added in the polymer matrix to improve specific properties) in polymer composites to replace conventional filler agents, such as carbon black and carbon fibers, for reinforcement purpose (Stankovich et al., 2006). More specifically, graphene oxide (GO) and reduced graphene oxide (rGO) are ideal for polymer composites due to their high dispersibility and the presence of functional groups that have chemical affinity to the surrounding polymers and increase filler/matrix adhesion (Ferrari et al., 2015; Stankovich et al., 2006). Several studies have shown that the addition of small GRM amounts (0.1–5%) can significantly enhance the strength, electrical conductivity or thermal transport of the composites compared to the neat polymer matrix (Zhao et al., 2010; Bortz et al., 2012; Song et al., 2011; Wang et al., 2015a, 2015b; Shi et al., 2018). Among the different polymer matrices, polyamide 6 (PA6, also known as Nylon-6), a widely used engineered thermoplastic polymer, has received great attention, as an ideal matrix for the development of graphene-reinforced polymer composites (Gong et al., 2015; Fu et al., 2015). Its attractive properties, such as good processability, heat and chemical resistance together with its beneficial mechanical characteristics, *i.e.,* stiffness and toughness, make PA6 appealing for composite applications (*e.g.,* automotive and sports equipment) (Fu et al., 2015; Mouhmid et al., 2006). Despite its exciting characteristics, PA6 has poor dimensional stability, low electrical conductivity, and weak mechanical performance in some areas, which can all be considerably improved by the use of GRMs as nanofillers (Xu and Gao, 2010; Pant et al., 2013; O'Neill et al., 2014).

Although GRMs may provide solutions to current challenges in many fields, the inevitable occupational or consumer exposure to these materials has raised scientific and public concern for their potential to affect human health. As a result, various studies have been initiated to assess the safety of GRMs in different biological systems, with the reported investigations often showing contradictory or inconclusive results. Several cellular and animal studies with different experimental setups have shown that different types of GRMs can induce mitochondrial dysfunction, cell apoptosis, genotoxicity, inflammatory or oxidative stress responses (Mittal et al., 2016; Chen et al., 2012; Li et al., 2018; Liu et al., 2013), while others reported the absence of adverse effects (Kucki et al., 2016, 2018; Drasler et al., 2018) as reviewed by Fadeel et al. (2018) Overall, this diversity in research outcomes indicate that GRMs are an incredibly diverse family of materials, whose safety thresholds is dependent on the complex interplay of several physicochemical properties such as lateral dimension, thickness, oxidative state, functional groups, dispersion state, purity, administrative doses, exposure route and duration (Wick et al., 2014; Ou et al., 2016). Despite the large number of studies addressing the potential impact of GRMs on human health, knowledge gaps on their structure-activity relationships remain. At present, no classification system exists to determine the exact level at which each material property may contribute to GRM toxicity. Thus, GRM hazard assessment prediction based on physicochemical characteristics is precluded.

It is further acknowledged that during the life cycle (production, use, disposal) of GRM-reinforced composites, possible degradation of the solid polymer matrix, *i.e.,* through mechanical abrasion, hydrolysis, water exposure, elevated temperatures or increased UV light intensity, can potentially lead to GRM release and subsequent unintentional exposure of workers and/or consumers (Froggett et al., 2014; Duncan and Pillai, 2015; Zepp et al., 2020; Lankone et al., 2020; Waquier et al., 2020). In contrast to pristine GRMs, which have been extensively studied, the nanosafety assessment of materials released from GRM-containing products have not been yet explored and only limited information is available about intrinsic hazards of dissociated materials from graphene-based composites. Moreover, GRMs used as nanofillers in composites may be transformed during the manufacturing process and/or during abrasion process in terms of their physicochemical characteristics such as lateral dimension, thickness, and defects. As a result, the transformed GRMs may cause different biological responses when compared to their pristine form.

The aim of the present study was therefore to investigate the

potential biological effects of particles released from a real-life GRM-enabled product (*i.e.*, rGO-reinforced PA6 composites that will be soon found in the vehicle industry) through an abrasion process, and compare these effects to those induced by the rGO initially incorporated in the PA6 thermoplastic polymer matrix. Since GRMs and nanomaterials in general, can enter the human body *via* different routes (*i.e.*, inhalation, ingestion, or dermal absorption) (Fadeel et al., 2018; Oberdörster et al., 2005; Pelin et al., 2018) we performed a multi-system and multi-endpoint *in vitro* human toxicity analysis (Fig. 1). Using well-established cell lines and cell-type specific endpoints, we first assessed the impact of abraded rGO-reinforced PA6 (PA6-rGO) composite materials on cells representative of key target organs related to the three main exposure routes (*i.e.,* lungs, gut, and skin), and the immune system, our primary defense mechanism against foreign intrusion. As inhalation of airborne materials is a major concern at the workplace where such GRM-enabled products are likely to be processed, we further assess the possible effects of PA6-rGO composite materials on the lungs after single pulmonary exposure in mice. Based on this tiered approach combining *in vitro* and *in vivo* data, the objective of the present study was to provide a comprehensive, multi-laboratory hazard assessment of commercial GRM-enabled products at doses expected at the workplace.

1. Materials and methods

1.1. Chemicals and reagents

All chemicals and reagents used were obtained from Merck-Sigma-Aldrich (Switzerland), unless otherwise stated.

1.2. Production and characterization of rGO and PA6/PA6-rGO composites

1.2.1. GO preparation

GO dispersion was prepared using the modified Hummers method, using natural graphite sieved at 60 and 100 mesh as described by Eckmann and colleagues (Carosio et al., 2018). The GO water dispersion was ultracentrifuge at 20.000 rpms in a SIGMA3–30 K ultracentrifuge, and the wet solid was collected and filtered off and air-dried.

1.2.2. rGO preparation and functionalization

GO powder was thermally reduced in argon atmosphere at 200ºC for 20 min. Aminopropyl silane functionalized rGO was prepared as follows; Ten g of rGO was suspended in a mixture of ethanol/water (30/70) and stirred for 1 h. Concentrated hydrochloric acid was added to adjust pH between 3 and 3.5. Five mL of (3-aminopropyl) triethoxysilane (APTES) were added and the mixture was stirred overnight at 60ºC. The suspension was vacuum filtered and washed with ethanol to avoid free silane molecules. The powder was dried at 80ºC for 24 h.

1.2.3. Preparation of PA6-rGO composites and characterization

For the preparation of the concentrated masterbatches, an Alphatech AD30mm LD48 counter rotating twin screw extruder was utilised. The functionalised rGO (2.5 wt%) was dispersed in PA6 by melt compounding, resulting in concentrated master batches. The screw speed was kept at 125 rpm and the feeder speed at 30 rpm.

The process temperature in the different barrels in extrusion processes are presented in Table 1.

The extruded material was then compression moulded to form the film for the abrasion.

Raman Spectroscopy. Raman spectra of rGO and composite materials (before abrasion) were acquired on a confocal RENISHAW in *via* Raman microscope at room temperature. The system uses a CCD detector and a holographic notch filter, using excitation wavelength of 532 nm. Scans were acquired from 1000 to 3500 cm^{-1}, performing maps of 25 spectra and making an average spectrum which is the one that is presented in this paper. Analysis and deconvolution of spectra were obtained with Wire 4.2 software.

X-ray Photoelectron Spectroscopy. XPS analysis was performed in a KRATOS Axis Ultra DLD.

Fourier-transform infrared spectroscopy. Infrared spectra were

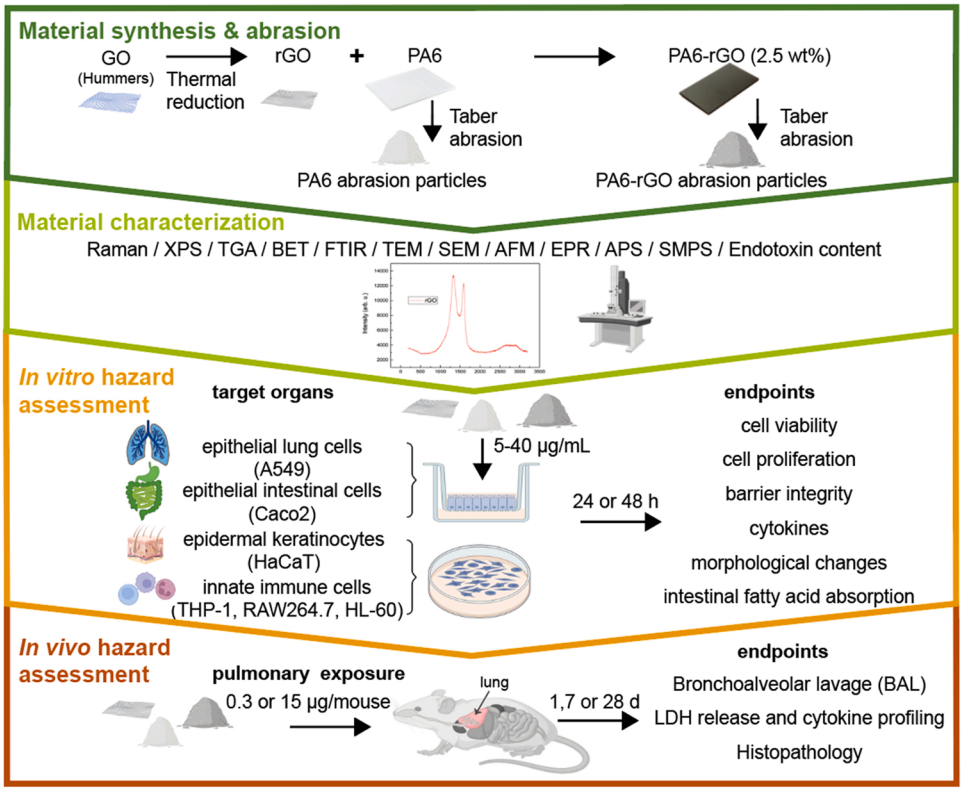

Fig. 1. Schematic overview of the experimental strategy. The main steps in the study include: 1) Material generation where rGO is produced by thermal reduction from GO dispersions synthesized by the modified Hummers method. Then, rGO is functionalized with aminopropyl silane and used to generate an industrially relevant rGO-reinforced polyamide 6 composite (PA6-rGO; 2.5 wt% rGO). Abrasion particles are produced from neat PA6 and PA6-rGO by Taber abrasion to mimic a mechanical abrasion. 2) Extensive material characterization is performed using a wide spectrum of analytical methods to support data interpretation and comparability across studies. 3) *In vitro* hazard assessment of the different materials is conducted in robust and widely used cell models representing potential key target organs including the lung, intestine, skin and immune system. 4) *In vivo* hazard is assessed in mice with a focus on short- and long-term toxicity in the lungs, representing the most relevant exposure route. Finally, all the data is carefully analysed in order to achieve a better understanding of the health hazard of abraded PA6-rGO *versus* rGO alone.
(parts of the figure were created with Biorender.com).

Table 1
Temperatures of the different extruder zones, during melt compounding.

Extruder zones	Z1	Z2	Z3	Z4	Z5	Z6	Z7	Z8	Z9	Z10
Temperature (°C)	190	190	210	210	210	220	220	220	220	230

recorded in the 4000–450 cm− 1 range using a PerkinElmer FT-IR Spectrum Two spectrometer.

Thermogravimetric analysis. TGA was performed in a METTLER TOLEDO TGA/SDTA 851e in the range of 25–900 °C 10°/min at air atmosphere.

Brunauer-Emmett-Teller. The specific surface area (SSA) of GRMs was determined by BET using an autosorb-6 Quantachrome instruments. The samples were degassed in an autosorb degasser (Quantachrome instruments) at 250 °C for 8 h.

Transmission electron microscopy. TEM were recorded using a JEOL microscope (JEM-2010). GRM samples were dispersed in isopropyl alcohol then sonicated with a Hielscher UP200S sonicator for 15 min and drop casted onto copper grids for TEM.

1.2.4. Characterization of rGO and abraded particles

Scanning Electron Microscopy. The morphology of rGO powder and abraded particles was characterised using an SEM Zeiss Evo50 microscope (acceleration voltage of 10 kV). The powders were deposited on conductive carbon tape and a thin layer of gold (≈ 10 nm) was sputter-coated on top of the samples.

Atomic Force Microscopy. AFM images were collected by a contact mode (Bruker, Dimension-Icon) to analyze the thickness of the tested materials. Images were obtained using ScanAsyst-Air probes (silicon tips on silicon nitride cantilever, Bruker) with 0.4 N/m nominal spring constant of the cantilever. For the AFM visualization, rGO, PA6 and PA6-rGO were dispersed *via* sonication (10 min) to ethanol. The rGO flakes were then coated to Si/SiO_2 (300 nm) substrate using spin coating method.

Optical Microscopy. For the optical measurements a Nikon Eclipse LV150N - Digital imaging combined with an advanced optical system was employed.

Raman Spectroscopy. Raman spectra of the samples were obtained using a Renishaw inVia Raman spectrometer equipped with a 514 nm laser. Four different spectra were acquired in different locations of the samples giving consistent results.

EPR spectroscopy. EPR spectra were recorded with an ESP 300E spectrometer (Bruker) operating at X-band and equipped with a high sensitivity resonator (4119HS-W1). Spectra were recorded with 2 mW microwave power, a modulation frequency of 100 kHz, a modulation amplitude of 0.1 mT, a conversion time of 81.92 ms and time constant of 20.48 ms.

Fluorescence spectroscopy. The presence of ROS in PA6, rGO and PA6-rGO dispersed in 0.1% BSA (at a concentration of 40 μg/mL) was assessed following the fluorescence changes of dihydrorhodamine 123 (DHR123, Sigma-Aldrich) signals using a Jasco FP8003 fluorimeter equipped with a swig xenon 450 W lamp. The non-fluorescent DHR123 is oxidized by ROS to fluorescent rhodamine 123 leading to a significant increase of photoluminescence. In a typical assay, PA6, rGO and PA6-rGO were prepared in 0.1% BSA (1.0 mg/mL) and stocked in the 4 °C for one week. Then, the stock solutions (80 μL) were diluted with a 0.1% BSA solution (1920 μL) to 40 μg/mL, following the addition of DHR123 (0.4 μL of a stock solution at 1 mM in DMSO) (final concentration of DHR123 corresponding to 200 nM). The fluorescence spectra were recorded immediately (<1 min) and 10 min after adding DHR123 under the excitation at 500 nm and were corrected for the baseline and the solvent. The fluorescence signal of 0.1% BSA following the addition of DHR123 was also tested at 0 min. A Fenton reaction was performed as a positive control. A 200 μL stock solution (10 mM) of the $FeSO_4.7\ H_2O$ was added to 1.6 mL of water followed by 0.4 μL of DHR123 (final concentration of DHR123 corresponding to 200 nM) and 200 μL H_2O_2. For this positive control, the fluorescence spectra were recorded immediately (<1 min) and 10 min after adding H_2O_2.

1.3. Abrasion process and particle collection

The abrasion process was performed as described by Netkueakul et al. Netkueakul et al. (2020) Briefly, PA6 and PA6-rGO composites were abraded using a Taber abraser (Model 5135, Taber, North Tonawanda, NY) equipped with a S-42 sandpaper strip wrapped around a CS-0 wheel with an applied weight of 1 kg to simulate the sanding process on the surface of the composites. The released particles were collected on 0.2 μm nucleopore filter (Whatman, UK) *via* a vacuum inlet (flow rate 10 lpm) with a small suction area of 40 mm^2, connected to conductive silicon tubing (TSI, United States).

Particle Size Distribution. The particle size distribution of the release particles was measured online using an APS (Model 3321, TSI) and a SMPS consisting of a differential mobility analyser (DMA) (Model 3080, TSI, Shoreview, MN) and a condensation particle counter (CPC) (Model 3775, TSI). The flow rate was generated by the vacuum line and monitored in the range of 9–11 L/min using a mass flow controller (Model GFM37, Aalborg, NY). In the present experimental setup, the APS analysed the aerodynamic diameter of particles in the range of 0.5–20 μm, while the SMPS analysed particles with electrical mobility diameter ranging from approximately 10 to 570 nm. At least three particle size distributions measurements were collected from each sample. The collection of abraded particles for nanosafety analysis and for further material characterization was performed without the APS and SMPS to reduce possible particle loss.

1.4. Material dispersion

For all experiments, freshly prepared stock dispersions of the tested materials (rGO, abraded PA6 and PA6-rGO particles) of 0.5 mg/mL in 0.1% bovine serum albumin (BSA) were prepared by sonication for 45 min prior to usage. Stock dispersions were diluted to the final working experimental concentrations (2.5–40 μg/mL) in complete cell culture medium and used immediately for exposure experiments.

1.5. Endotoxin content

1.5.1. Endotoxin Chromogenic assay

The endotoxin concentration in PA6, PA6-rGO and rGO suspensions was measured using the Pierce™ LAL Chromogenic Endotoxin Quantitation kit (sensitivity 0.1 EU/mL; Thermo Fisher Scientific, MA, USA), following the manufacturer's instructions, at concentrations 0–80 μg/mL.

1.5.2. TET Assay

PA6, PA6-rGO, and rGO samples were assessed for endotoxin content with the TNF-α expression test (TET), which enables unequivocal detection of endotoxin with a sensitivity comparable to that of the conventional LAL assay but without any interference with the assay. In brief, PBMCs were isolated from buffy coats obtained from healthy human blood donors (Karolinska University Hospital, Stockholm, Sweden) by density gradient centrifugation, as described previously (Fadeel et al., 1998). Then, PBMCs were positively selected for CD14 expression with CD14 MicroBeads (Miltenyi Biotech, Bergisch Gladbach, Germany). For obtaining HMDMs, CD14 + monocytes were cultured in RPMI-1640 cell medium supplemented with 2 mM L-glutamine, 100 IU/mL penicillin, 100 mg/mL streptomycin, and 10% heat-inactivated

fetal bovine serum (FBS), supplemented with 50 ng/mL recombinant macrophage colony-stimulating factor for 3 days in 96-well plates. HMDMs were exposed to PA6, PA6-rGO, and rGO (20 μg/mL) or to bacterial LPS (0.01 μg/mL) (Sigma-Aldrich) in the presence or absence of the specific LPS inhibitor, polymyxin B (10 μM) (Sigma-Aldrich), and TNF-a secretion was measured at 24 h of exposure with a Human TNF-α ELISA Kit purchased from MABTECH (Nacka Strand, Sweden).

1.6. Detection of released graphene from PA6-rGO abraded composites

1.6.1. Freeze fractured samples and SEM visualization

As the release of rGO could be explained by the debonding of the rGO from the PA-6 matrix, freeze fractured method was employed to simulate the debonding process and to explain the debonding mechanism. In order to generate the freeze fractured surface, the sample was immersed into liquid nitrogen for 30 s. After removing the sample from liquid nitrogen, the sample was immediately broken by manual bending. Freeze fractured surface of the samples was analyzed using scanning electron microscope (Nova NanoSEM 230, FEI company, Hillsboro, OR, USA).

1.6.2. Transmission electron microscopy of abraded PA6-rGO

It was important to evaluate whether abrasion process could induce the release of the rGO from the polymer matrix or not. If the rGO can be released, it is also crucial to assess in which forms rGO was released. Therefore, to understand the characteristics of rGO in the abraded PA-6-rGO, the abraded PA6-rGO was analyzed using TEM (FEI Tecnai G2 F20 (FEI Company, OR, USA)).

2. *In vitro* experiments and post-exposure biological response

2.1. Cell cultures

2.1.1. Lung cultures

Human A549 epithelial type II cells were obtained from American Type Culture Collection (ATCC; Virginia, USA). After thawing, A549 cells were sub-cultured in T75 cell culture flasks in complete Rosewell Memorial Park Institute medium (RPMI-1640, Sigma-Aldrich) with 10% FBS (Sigma-Aldrich), 1% penicillin, streptomycin, neomycin (PSN; Sigma-Aldrich) and 1% L-glutamine (Sigma-Aldrich). Cells were maintained at 37 °C and 5% CO_2 in humidified atmosphere and were routinely sub-cultured twice a week at 70–80% confluence.

Prior to the experiments, cells were seeded apically on transparent polycarbonate 12-well inserts (3 μm pore size, 113.1 mm^2 surface area, Greiner Bio-One, Austria) at concentration of 2.5×10^5 cells/insert and were grown for three days on submerged conditions to form a tight monolayer, Cell cultures were then transferred to air-liquid interface (ALI) conditions by removing the apical medium in order to produce surfactant and better reflect *in vivo* conditions in human lung (Chortarea et al., 2015). After 24 h at ALI, cells were then exposed apically to 100 μL of different concentrations of PA6, PA6-rGO and rGO (2.5–40 μg/mL), for 24 h and 48 h (pseudo-ALI approach (Barosova et al., 2018; Endes et al., 2014)).

Crystalline quartz DQ (purchased from Dörentrup Quarz GmbH & Co. (material No. 04; mean particle diameter d(50)= 3.71 μm, d(97)= 12.03 μm)) was included as a positive inflammogenic control for A549 cells. DQ was freshly dispersed in ultrapure ddH_2O, and 100 μL were applied apically in A549 cells (final concentration of 100 μg/mL).

2.1.2. Skin cultures

HaCaT cells were cultured in high glucose Dulbecco's Modified Eagle's medium (DMEM), supplemented with 10% FBS, 1.0×10^{-2} M L-glutamine, 1.0×10^{-4} g/mL penicillin and 1.0×10^{-4} g/mL streptomycin at 37 °C in a humidified (95%; air: 5% CO_2) atmosphere. Cell passage was performed two days post-confluence, once a week. All the experiments were performed between passage 74 and 86. For cytotoxicity assays, cells were seeded in flat bottom 96-well plates at a density of 5×10^3 cells/well and exposed to different concentrations of the tested materials (2.5–40 μg/mL) for 24 h and 48 h. Before each assay, cells were washed twice with phosphate buffered saline (PBS).

2.1.3. Intestinal cultures

The human colorectal adenocarcinoma cell line Caco-2 was obtained from the German collection of microorganisms and cell cultures (DSMZ, Braunschweig, Germany). Cells were maintained in Minimum Essential Medium (MEM; Sigma-Aldrich) supplemented with 10% FBS, 2 mM L-glutamine (Sigma-Aldrich), 1% PSN (Sigma-Aldrich) and 1% non-essential amino acids (Sigma-Aldrich) Cell cultures were maintained at 37 °C, 5% CO_2 and 95% humidity and routinely sub-cultured twice a week at 70–80% confluence using 0.5% trypsin–EDTA (Sigma-Aldrich).

Differentiation of intestinal cells. Caco-2 cells were seeded at a density of 250,000 cells/well (corresponds to 2.2×10^5 cells/cm^2), in Thin-Cert™ cell culture inserts for 12-well plates (high pore density transparent PET membrane, with 3 μm diameter pore size; Greiner bio-one, Kremsmünster, Austria). Cells were grown for 21 days to obtain mature differentiated monolayer and cell culture medium was refreshed three times per week. At day 22, cells were treated with different concentrations of the tested materials at a range of 2.5–40 μg/mL (100 μL of particle suspension, added apically), for 24 h and 48 h.

2.1.4. Immune cell cultures

The human monocytic THP-1 cell line was purchased from the ATCC (Virginia, USA). Cells were grown in RPMI 1640-GlutamaxTM-I media containing HEPES (Gibco, Sweden) and supplemented with 100 U/mL penicillin, 100 mg/mL streptomycin and 10% heat-inactivated FBS (Sigma). The cells were passaged at a cell density of up to maximum 8.0×10^5/mL every 3–4 days.

Differentiation of THP-1 cells. For the experiments, the THP-1 cells were plated at the cell density of 60,000 cells/well and pre-incubated for 24 h in the presence of 0.5 μM PMA, as described previously (Bhattacharya et al., 2017). After 24 h the differentiated THP-1 cells were washed with luke-warm sterile PBS and exposed to rGO, PA-6-rGO and PA-6 (concentrations 5–40 μg/mL) for 24 h. Cells were tested regularly using MycoAlert® mycoplasma detection kit (Lonza, Basel, Switzerland). Cells were seeded in 96-well plates in RPMI-1640 medium at a density of 60000 cells/well and subsequently exposed to the tested materials at concentrations 5–40 μg/mL for 24 h, or were maintained in cell medium alone (untreated cells-negative control).

The RAW 264.7 macrophage cell line was cultured in DMEM cell culture medium supplemented with 10 μg/mL gentamycin, 10 mM *N*-(2-hydroxyethyl)-piperazine- *N*-ethanesulfonic acid, 0.05 mM β-mercaptoethanol and 10% FBS at 37 °C in a 5% CO_2 incubator. Cells were seeded in 96-well plates at a density of 1×10^4 cells per well and cultured for 24 h prior the material exposure.

The human acute promyelocytic leukemia cell line HL-60 (ATCC – CCL-240) was maintained in phenol red-free RPMI-1640 medium supplemented with 2 mM l-glutamine and 10% heat-inactivated FBS (Sigma) in 5% CO_2 at 37 °C.

Differentiation of HL-60 cells. In order to allow for neutrophil-like differentiation, the cells were seeded at 0.5×10^6 cells/mL in the above-mentioned cell medium supplemented with 1.25% DMSO for 5 days, as described previously (Khandagale et al., 2018). The culture medium was refreshed after 3 days. Cells were tested regularly using MycoAlert® mycoplasma detection kit (Lonza, Basel, Switzerland). Prior the exposure, experiments the differentiated HL-60 cells were seeded in 96-well plates in phenol red-free RPMI-1640 medium at a density of 60000 cells/well.

After seeding, the immune cells were treated with the indicating concentrations (5, 10, 20, 40 μg/mL) of PA6, PA6-rGO and rGO and the biological response was evaluated 24 h post-exposure.

2.2. Cell viability

2.2.1. MTS assay

The effects of the materials on cell viability were evaluated by the 3-(4,5-dimethylthiazol-2-yl)− 5-(3-carboxymethoxyphenyl)− 2-(4-sulfophenyl)− 2 H-tetrazolium (MTS) assay (CellTiter 96® AQueous One Solution Cell Proliferation Assay, Promega, Dübendorf, Switzerland) in all the cell models examined (with the exception of the neutrophil model, where the ATP assay was performed instead), according to ISO 19007:2018 and (Elliott et al., 2017). Briefly, after material exposure, phenol red free fresh medium containing the MTS reagent was added to the cells. Then, the cell cultures were incubated for an additional 1 h (4 h for the skin model), at 37 °C. Absorbance was measured at 490 nm by a microplate reader. The chemical positive control cadmium sulphate ($CdSO_4$, Sigma-Aldrich) was added to the cells at concentration 1000 μM for 24 h. Data are presented as % cell viability as compared to negative control (untreated cells).

Cell free interference assay was performed for the rGO and the abraded particles, at a concentration range of 0–40 μg/mL to exclude potential interference reactions of the tested materials with the MTS assay reagents along that might lead to possible wrong interpretation of the results (SI 15).

2.2.2. ATP assay

The ATP assay was performed for the viability assessment of the neutrophil model. After the 24 h material exposure, the differentiated HL-60 cells were lysed, and total cellular ATP content was quantified with a luminescence-based cell viability assay, CellTiter-Glo (Promega, Dübendorf, Switzerland). CellTiter-Glo reagent was mixed at a 1:1 ratio with the experimentally treated cells from the treatment plate. The mix was incubated for 10 min at room temperature on the shaker, followed by luminescence measurement with an Infinite F200 Tecan plate reader (Mannendorf, Switzerland). The experiment was performed with at least three biological replicates and three technical replicates for each concentration of PA-6, PA6-rGO, and rGO. Results were expressed as percentage cell viability *versus* control.

To control for potential interference of the materials with the assay, the PA-6, PA6-rGO and rGO were dispersed in cell-free medium (at the working concentrations) and mixed with CellTiter-Glo reagent (no interference was observed; data not shown).

2.2.3. WST-8 assay

The cell viability in skin cells was additionally evaluated by the 2-(2-methoxy-4-nitrophenyl)− 3-(4-nitrophenyl)− 5-(2,4-disulfophenyl)− 2 H-tetrazolium (WST-8) reduction assay. The WST-8 assay was carried out using the Cell Counting Kit (CCK)− 8 assay (Sigma Aldrich; Milan, Italy), as previously described (Pelin et al., 2018). Briefly, after materials exposure and two washings with PBS, cells were incubated for 4 h with fresh medium containing 10% WST-8 reagent. Absorbance was determined at 450 nm by an Automated Microplate Reader EL 311 s (Bio-Tek Instruments; Winooski, VT). Data are reported as % cell viability as compared to negative control (untreated cells).

2.2.4. LDH assay

The potential cytotoxicity in RAW 264.7 macrophages was assessed by the LDH test kit (CytoTox 96® Non-Radioactive Cytotoxicity Assay, Promega, Dübendorf, Switzerland), according to the manufacturer's instructions. Following the 24 h post-exposure time, the culture medium was collected for the LDH measurements. Treatment of cells for 30 min with lysis solution (included in the assay) was served as positive control to induce cytotoxicity. The OD of each sample was recorded at 490 nm on a Microplate Reader (Thermo, Varioskan Flash). LDH release (% of positive) is presented as the percentage of $(OD_{test}\text{-}OD_{blank})/(OD_{positive}\text{-}OD_{blank})$, where OD_{test} is OD of control cells or cells exposed to materials, $OD_{positive}$ is OD of positive control cells and OD_{blank} is OD of well without cells.

2.3. Evaluation of intestinal barrier integrity

The differentiation process of Caco-2 cultures grown in 12-well inserts was controlled by TEER measurements at day 7, 14 and 21 after seeding using an Epithelia Voltohmmeter (EVOM) with sterilised STX2 electrodes (World precision, Instruments, Sarasota Florida, USA). The impact of different concentrations of PA6, PA6-rGO and rGO (2.5–40 μg/mL) on the barrier integrity of differentiated Caco-2 cells was assessed by measuring the TEER before the treatment (0 h) and after 24 h and 48 h of treatment. Three measurements in different parts of the insert were retrieved from each sample, and TEER values were calculated using the formula TEER = [Ω (cell inserts) – Ω (cell-free inserts)] × 1.12 cm^2. The values for each concentration represent the average of three independent experiments.

2.4. Lipid absorption on the intestinal barrier

To investigate the potential effects of rGO and abraded PA6/PA6-rGO particles on lipid uptake, differentiated Caco-2 cells on 12-well inserts were exposed with different concentrations of each tested material (5–40 μg/mL) for 24 h and 48 h. Cell cultures treated with 50 μg/mL of the fatty acid synthase inhibitor C75 for 24 h were used as a positive control. Lipid uptake was measured as described in previous work (Hempt et al., 2020). Briefly, after material exposures, the cultures were incubated for 10 min with 20 μM BODIPY™ 500/510 C1, C12 (Thermo Fischer, D3823) in 0.1% BSA, according to the manufacturer's instructions. Then, the inserts were washed with ice cold 0.1% BSA and complete DMEM medium (phenol red free) was added to the apical and basolateral side. After 1 h incubation at standard growth conditions, the fluorescence was measured with a multi-well plate reader (Mithras2 Plate reader, Berthold Technologies, Germany) at 485/528 nm (excitation/emission).

2.5. Skin cell mass and proliferation

Cell mass was evaluated by the sulforhodamine B (SRB; Sigma Aldrich, Milan, Italy) assay, as a measure of viable adhered cells (Pelin et al., 2017). Briefly, after materials exposure, cells were washed twice with PBS, fixed with 50% trichloroacetic acid for 1 h at 4 °C and stained for 30 min with 0.4% SRB in 1% acetic acid. After washings with 1% acetic acid, the protein-bound dye was dissolved in 10 mM TRIZMA base solution and the absorbance was read by an Automated Microplate Reader EL 311 s (Bio-Tek Instruments, Winooski, VT, USA) at 570 nm. Data are reported as % of cell mass with respect to negative control.

Cell proliferation was evaluated using a colorimetric ELISA based on 5-bromo-2′-deoxyuridine (BrdU) incorporation (Sigma-Aldrich; Milan, Italy), following the manufacturer's instructions. Absorbance was read by an Automated Microplate Reader EL 311 s (Bio-Tek Instruments, Winooski, VT, USA) at 450 nm. Data are reported as % of cell proliferation with respect to negative control.

2.6. Inflammatory responses (lung and immune cells)

2.6.1. Cytokine and chemokine release

The secretion of human IL-6 and IL-8 in A549 alveolar epithelial cells (24 h and 48 h post-exposure to rGO and abraded composite materials) was quantitatively detected by enzyme-linked immunosorbent assay (ELISA; Human IL-6 and IL-8 Uncoated Elisa Kit, Invitrogen, USA) according to manufacturer's instructions. Cells treated apically with 1 μg/mL TNF-α for 24 h were used as positive control. Measurements were performed on high binding 96-well plates (Coating Costar, New-York, USA) and at 370 nm optical absorbance using a microplate reader (Mithras 2 Plate Reader, Berthold Technologies, Germany).

Differentiated THP.1 were exposed to rGO (20 μg/mL). The exposed cell media were collected and stored at − 80 °C for further analysis. IL-1β release was determined by using a human IL-1β ELISA kit (Invitrogen,

Sweden) according to the manufacturer's instruction. Absorbance was measured at 450 nm using a Tecan Infinite F200 plate reader. Results are expressed as pg/60 000 cells of released cytokine. To assess the role of the NLRP inflammasome, cells were preincubated for 1 h with either zVAD-fmk (20 μM) and MCC950, an NLRP3 inhibitor (10 μM) (both from Sigma).

The release of TNF-α (BD OptEIA, BD Biosciences) and IL-6 (BD OptEIA, BD Biosciences) in RAW 264.7 macrophages, following 24 h treatment with the tested materials was determined using ELISA kits (BD Biosciences), following the manufacturer's instructions. Optical absorbance measurements were performed using a microplate reader (Thermoscientific, VARIOSKAN LUX) at 450 nm. LPS (1 μg/mL for 24 h, Sigma) served as the positive control to stimulate inflammatory response.

2.6.2. Multiplex analysis-based cytokine profiling on immune cells

The Meso Scale Discovery (MSD) (Rockville, MD, USA) plate-based electrochemiluminescence (ECL) assay was employed to quantify cell supernatant concentrations of IFN-γ, IL-1β, IL-2, IL-4, IL-6, IL-8, IL-10, IL-12 p70, IL-13, and TNF-α. As a positive control, cells were exposed to 0.1 μg/mL LPS for 24 h. The stored cell supernatant was thawed on wet ice just prior to use. Samples were diluted 1:2 using Diluent 2, and each sample was run in duplicate. The V-PLEX Human Pro-inflammatory Panel 1 Human Biomarker 10-Plex Kit was used. Plates were processed according to the manufacturer's instructions and read using the MSD MESO Sector S 600 instrument. The assay data were analyzed using MSD Discovery Workbench 4.0. The cytokine expression data retrieved from the multiplex assay were analyzed using hierarchical clustering analysis. Complete linkage and Euclidean distances were employed as metrics to draw association dendrograms between cytokines and the different treatment conditions, as described previously (Bhattacharya et al., 2017). The cluster analysis and the corresponding heat maps were prepared by using R, as previously reported (Bhattacharya et al., 2017).

2.7. Cell morphology

Following the 24 h and 48 h material exposure, A549 alveolar epithelial cells were fixed in 4% paraformaldehyde (PFA) and incubated at 4 ^{o}C. In order to prepare the cells for staining, cultures were incubated with 0.1 M glycine in PBS for 15 min. Then, cells were permeabilized with 0.2% Triton X-100 in PBS for another 15 min, prior the application of fluorescent dyes. DAPI (4′,6-diamidino-2-phenylindole) (Thermo Fischer, USA), and Alexa Fluor 488 (Thermo Fisher, USA) were used to stain nuclei and cytoskeleton of the cells respectively. DAPI and Alexa Fluor 488 were diluted to ratio of 1:1000 and 1:50 respectively in 0.3% Triton X-100 and 1 g BSA in PBS. Following the staining, cells were incubated with fluorescent dyes for 1.5 h in darkness, at room temperature. Subsequently, cells were washed three times with PBS and mounted on microscopy slides using Mowiol® 4–88 (Sigma-Aldrich) on both sides of the membranes. Visualization of the cellular morphology was achieved using a confocal LSM fluorescence microscope (CLSM, LSM780, 60 × magnification oil, Carl Zeiss AG, Switzerland).

The morphology of keratinocytes was evaluated by confocal microscopy after membranes staining with 1 μM 1,1'-Dioctadecyl-3,3,3',3'-tetramethylindocarbocyanine perchlorate (DiL) probe (Sigma-Aldrich; Milan, Italy), as previously described (Pelin et al., 2017). Cells (2 $\times 10^5$ cells/well) were cultured for 24 h before exposure to each material (40 μg/mL) for 48 h. Cells were then washed twice with PBS, probed with 1 μM DiL for 10 min at room temperature, fixed with 4% PFA for 30 min at room temperature and washed twice with PBS. Samples were mounted on coverslips of 1 mm thickness using the Prolong Gold antifade reagent (Life Technologies; Milan, Italy). Images were taken by a confocal microscope (Eclipse C1si, on an inverted microscope TE2000U, Nikon) at 60 × magnification. GBMs presence in each sample was visualized by the reflection mode property during the confocal acquisitions. Reconstructions of the images were performed offline using the image-processing package Fiji.

RAW 264.7 macrophages were plated in the 96-well plates (1 $\times 10^4$ cells per well) and incubated for 24 h. Abraded materials were added to the cells at increasing concentrations (5, 10, 20, 40 μg/mL) upon dispersion in cell culture medium. Untreated cells cultured in cell culture medium in absence of materials were used as negative control. The cell morphology was observed under an optical microscopy (Zeiss Axiovert 40 CFL, 20 × magnification) at 24 h post-exposure.

3. *In vivo* exposure experiments and post-exposure tissue analyses

3.1. Animal husbandry

Prior to any experiment, C57BL/6 female mice (Envigo, UK) of 6–8-week old were acclimatized for 7 days after arrival. Animals were kept randomized in groups of 5 with free access to water and food, at a temperature of 19–22 °C, relative humidity of 45–65%, under a regular 12 h light/dark cycle between 7 am and 7 pm. All procedures were conducted in accordance with the ARRIVE guidelines for animal research and after ethical approval from the UK Home Office, under Project License no. P089E2E0A.

3.2. Animal exposure

All materials were prepared on the day of exposure by dispersion in water (water for injection, ThermoFisherScientific, Gibco) containing 0.1% BSA (Merck, Sigma-Aldrich). After anesthesia with 3% of isoflurane, mice were maintained on a slanted board and 30 μL of materials or vehicle was put at the basis of the tongue, allowing distribution of the materials into the lungs through physiological breathing. Mice (n = 3) were exposed by oropharyngeal aspiration to 15 μg (in 30 μL) of PA6-rGO (2.5% of rGO, which represents about 0.3 μg of rGO for 15 μg of PA6-rGO) or controls: neat PA6 (15 μg), rGO-0.3 μg (low dose, representing approximately 2.5% of the high dose) or rGO-15 μg (high dose) and vehicle (0.1% BSA in water). The applied dose of 15 μg per animal equals to 0.75 mg/kg, while 0.3 μg per animal equals to 0.015 mg/kg for animal weighing on average 20 g at the time of exposure. Outcomes were assessed at 1, 7, and 28 days after single exposure. At each time point, mice were euthanized by intraperitoneal injection with an overdose of pentobarbitone.

3.3. Bronchoalveolar lavage (BAL) analysis

At the end of the post-exposure recovery period, bronchoalveolar lavages (BAL) were performed on the right lung (isolated *via* litigation of the right bronchia) using 3 times 0.8 mL ice cold PBS (Merck, Sigma-Aldrich). BAL fluids were analyzed for composition in cell population (differential counting by Kwik-Diff Stains, Epredia, Shandon), LDH (LDH colorimetric assay, Promega) and total protein content (Bi-cinchoninic Acid (BCA) assay, Pierce BCA Protein Assays, ThermoFisherScientific). IL-6 and TNF-α concentrations in BAL fluids were assessed using Mouse ELISA MAX deluxe Sets (Biolegend).

3.4. Whole lung inflammation profile analysis

After BAL, the right lungs were lysed in RIPA buffer (Merck, Sigma-Aldrich) containing EDTA-free protease inhibitor (cOmplete Mini, Roche). After homogenization using 5 mm stainless steel beads for 10 min at 50 Hz (TissueLyser LT system, Qiagen), cell lysates were centrifuged for 5 min at 2600 g to remove cell debris. Collected supernatants were stored at −80 °C until analysis. Total protein concentrations were measured using a BCA assay (ThermoFisherScientific, Pierce), and cytokine levels were evaluated using a Mouse Inflammation Panel (13-plex: IL-1α, IL-1b, IL-6, TNF-α, MCP-1, GM-CSF, IL-17A, IL-23, IL-12p70, IFN-γ, IFN-β, IL-27 and IL-10, v-plate, Biolegend) following

manufacturer's recommendations. A FACSVerse flow cytometer (BD biosciences) was used to measure fluorescence intensities. Sample concentrations were determined using a standard curve and then expressed in pg/mg of protein after normalization by total protein concentration. IL-12p70 values were below the test sensitivity and were not considered.

3.5. Histopathological analysis

The left lungs were collected, fixed in formalin, paraffin embedded, sectioned on microtome, and finally stained using Hematoxylin and Eosin stain for further histopathological analysis.

3.6. Statistical analysis

In vitro results are presented as the mean ± standard error of the mean (SEM) of at least 3 independent experiments, and presented as the mean ± standard deviation for *in vivo* experiments (n = 3). Statistical analysis was performed by one-way ANOVA followed by Bonferroni's post-test, Dunnett's or Sidak's multiple comparison test analysis, using the software GraphPad Prism (version 9.0). The results were considered significant if $p < 0.05$. For each *in vivo* time point, Kruskall-Wallis followed by Dunn's post-hoc test was used to evaluate statistical differences compared to the negative control; $p < 0.05$: * .

4. Results and discussion

4.1. Characterization of rGO and abraded particles from PA6-rGO composites

The rGO samples were produced by thermal reduction from GO dispersions synthesized using the modified Hummers method (Carosio et al., 2018). Subsequently, rGO was functionalized with aminopropyl silane. The surface functionalization of rGO was verified by Raman, x-ray photoelectron spectroscopy (XPS), thermogravimetric analysis (TGA), Brunauer-Emmett-Teller (BET) and Fourier-transform infrared (FTIR) analysis. SI 1a presents a comparison of the Raman spectra of the GO, non-functionalized rGO and aminopropyl silane functionalized rGO). An intense D peak (~1350 cm^{-1}) which confirmed lattice distortions and the G peak (~1585 cm^{-1}) which corresponds to the overlap of G and D' peaks are observed. The 2D peak (~2700 cm^{-1}), and D+D' and 2D' peaks which are different overtone and combination peaks of the previous ones, show minimal intensity, corresponding to stage 2 defects. Non-functionalized rGO shows the highest I(D)/I(G) [I(D)/I(G) 1,15 (functionalized rGO), 0,70 (non-functionalized rGO), 0,86 (GO)] in agreement with the evolution of I(D)/I(G) in stage 2 of defects. A decrease in full width half maximum (FWHM) of D and G peaks were observed for non-functionalized rGO material $FWHM_G$: 73 (GO), 103 (non-functionalized rGO), 70 (functionalized-rGO) cm^{-1}; $FWHM_D$: 107 (GO), 186 (non-functionalized rGO), 78 (functionalized-rGO) cm^{-1}, which is associated to a decrease in disorder and in alignment with a decrease of the oxygen content due to a reduction process during the functionalization of rGO (Gómez et al., 2017; Eckmann et al., 2013; Beams et al., 2015). The reduction process was further confirmed by XPS where a decrease in the oxygen content was reported: 30.4% (GO), 13.5% (non-functionalized rGO), decreased to 6.7% (functionalized rGO), during the silanization process (SI 2). It should be noted, that the rGO is intentionally a partially rGO, because this characteristic (together with the functionalisation) enables a better integration and improved mechanical properties in the polymer composite for automobile applications. Hence, this rGO is not representative of graphene that would be used in electronics or for conductivity purposes. In the case of functionalized rGO, 0.4% of Si and 0.44% of N was observed corresponding to a 0.4% of functionalization of the rGO. FTIR spectra of the functionalized rGO in region 620–1300 cm^{-1} showed two width and high intensity peaks, which involved different components typically assigned to Si-O-Si, Si-O-C (1083 and 1047 cm^{-1} is typically assigned to the Si-O-C and Si-O-Si bonds, respectively, and indicates the successful chemical functionalization) and Si-C vibrations (appears at 870 cm^{-1} as broad peak) (SI 1b). Similar patterns were observed by Wan et al. Wan et al. (2014) TGA revealed a mass loss of 3.9 wt% below 525ºC, in agreement with the 4.3 wt% loss calculated when assuming a degree of functionalisation of 0.4% (SI 3). The starting non-functionalized rGO showed a BET surface area of 736,3 m^2/g, while the functionalised rGO incorporated in the composites, demonstrated a BET surface area of 178,7 m^2/g. The reduction in the surface area is attributed to the non-accessible area of the gases due to the stacking during the filtration and drying process (Guo et al., 2014). Transmission electron microscopy (TEM) observed that the functionalized rGO comprised of folded structures and was agglomerated (SI 4). The functionalized rGO was either embedded in the PA6 composites (2.5 wt%) or used for further characterization and toxicological analysis (hereafter, rGO refers to functionalized rGO).

The morphology of the rGO and the abraded composites (PA6 and PA6-rGO) was studied using scanning electron microscopy (SEM), atomic force microscopy (AFM), as well as optical microscopy (Fig. 2a, SI 5a-b). The SEM micrographs of the rGO showed aggregated nanoflakes with broad cluster sizes that range from 10 to 100 μm (Fig. 2a). Such an arrangement of graphene sheets is typical of rGO powders (Ali et al., 2017). Moreover, the large SEM magnification allows distinguishing crumpled nano-scaled flakes of rGO stacked together. The abraded PA6 particles form a worm-like structure with morphologies comparable to other previous reports (Golchin et al., 2013). The abraded PA6-rGO composites display similar worm-like topography with worm sizes in the range of 10–100 μm. The presence of rGO could not be detected by SEM imaging in the abraded PA6 particles. Similarly, Sachse et al., observed that particles generated from PA6-foam glass crystal (FGC), PA6-SiO_2 composites after a drilling process, showed very similar structures of particles (Irfan et al., 2013).

AFM was employed to evaluate the thickness of the flakes/agglomerates in the tested materials. Height profiles indicated areas of increased thickness of rGO flakes, which are predominantly stacking or folding on each other (SI 5a). Similarly, in the abraded PA6-rGO, the stacking of several layers was monitored, which is verified by the variation in thickness values. The average thickness for rGO and PA6-rGO was similar (6–10 nm and 4–10 nm, respectively). In addition, AFM showed that lateral dimensions of rGO ranged from 1 to 5 μm, while PA6-rGO ranged from 0.75 to 5 μm. Due to difficulties to disperse PA6 to a non-aggressive solvent, it was not possible to achieve AFM measurements for the neat PA6.

The presence of rGO in the PA6-rGO composite, after the abrasion process could be confirmed by the presence of the characteristic D and G peaks in the Raman spectra. The Raman spectra of the neat abraded PA6 particles presented a strong fluorescence contribution (Fig. 2b). The main peaks of this sample and the correspondent vibration modes were analysed in a previous report (Ferreiro et al., 2004). The Raman spectra of the rGO and abraded PA6-rGO were analysed through Lorentzian fitting. The rGO showed the typical D peak at approximately 1335 cm^{-1} and the G at ≈ 1579 cm^{-1}, which is consistent with previous studies (Fig. 2b) (Krishnamoorthy et al., 2012; Song et al., 2015). The I(D)/I(G) ratio was ≈ 1.2. The characteristic 2D peak could be observed between 2500 and 2800 cm^{-1}. The abraded PA6-rGO composite instead presented a blue shift of approx. 10 cm^{-1} resulting in a D peak at ≈ 1345 cm^{-1} and a G at 1587 cm^{-1} (I(D)/I(G) was ≈ 1.1).

The presence of surface radicals was examined by EPR and fluorescence spectra analysis as reactive oxygen species (ROS) account one of the main drivers for particle toxicity (Nel et al., 2006). As reported in the SI 6a, no radicals were observed in the neat PA6, while low amounts of radicals were detected in the rGO containing samples (both powder and dispersed form) with likely no influence on the biological responses in the concentrations tested (SI 6b).

The particle size distribution of the abraded composites was measured online, during the abrasion process, using the aerodynamic particle sizer (APS) and the scanning mobility particle sizer (SMPS) that

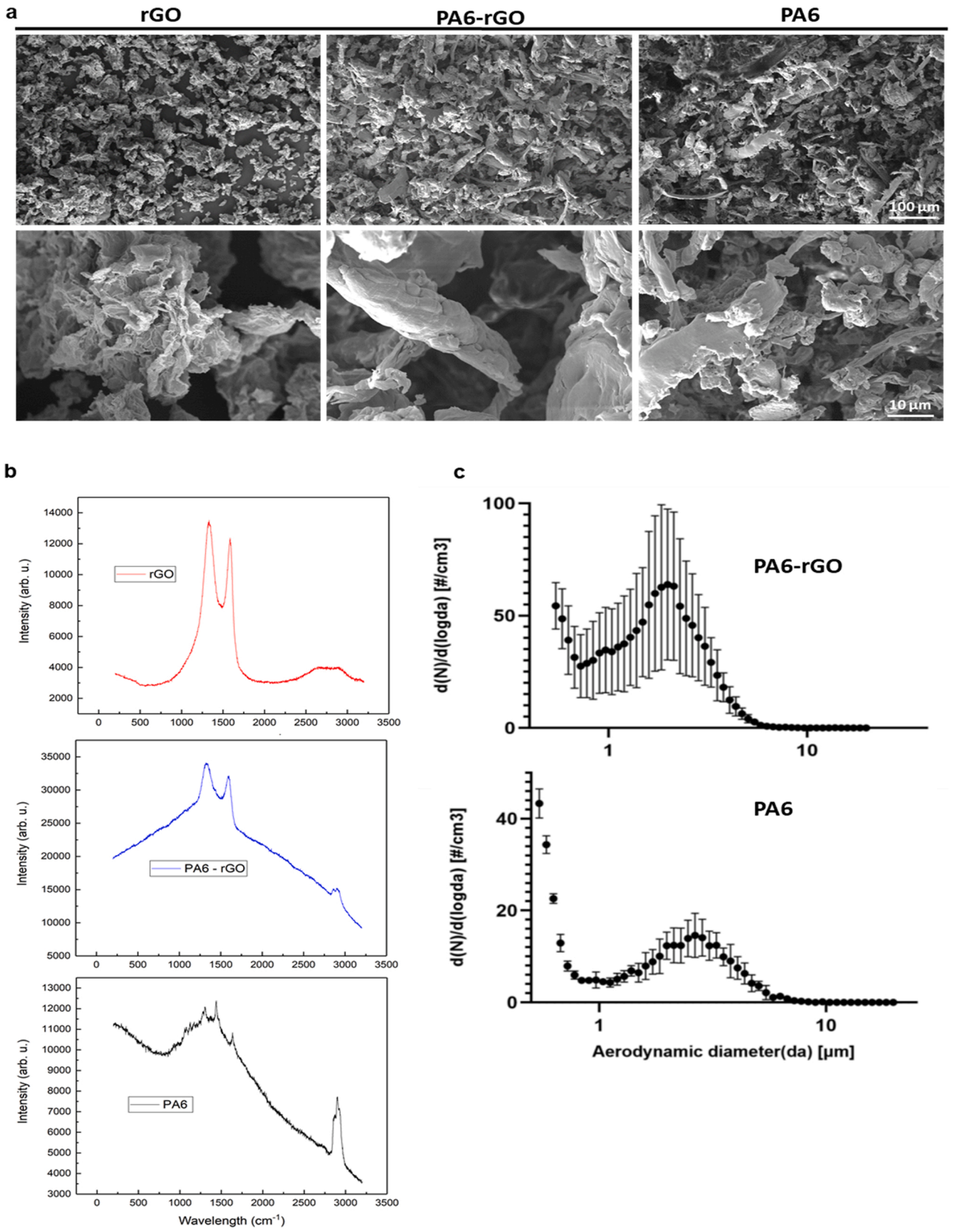

Fig. 2. Characterization of rGO and abraded particles from PA6-rGO composites. (a) SEM images of rGO, abraded particles from PA6-rGO composite and abraded particles from neat PA6. (b) Raman spectra of the tested materials (rGO, abraded PA6-rGO and abraded PA6). (c) Particle size distributions of the abraded particles in the micrometer range, measured by APS. The results show mean ± S.D. from at least three independent measurements.

quantify the aerodynamic diameter and the electrical mobility of the abraded particles, respectively. Online APS measurements of the released particles during the abrasion process revealed a mean aerodynamic diameter of 3.16 μm for the neat PA6 and 1.91 μm for the PA6-rGO composite particles (Fig. 2c). For both abraded materials, the obtained aerodynamic diameter values were under 4 μm, which falls into the respirable fraction in the alveolar region (Oberdörster et al., 2005). More specifically, particles with an aerodynamic diameter smaller than 100 μm can be inhaled, but only particles with an aerodynamic diameter smaller than 4 μm can reach the alveolar region of the lung (Oberdörster et al., 2005; Su et al., 2016). Another peak was observed towards the lower detection limit of the instrument (at 0.5 μm) for both abraded materials, indicating the presence of particles with an aerodynamic diameter smaller than 0.5 μm. It should be noted that the aerodynamic diameter of the abraded particles measured by APS was notably smaller than the particle size estimated by the SEM. This observation, which was reported previously by Schinwald et al., could be explained by the fact that in contrast to the particle size estimated by SEM from the projected area, the aerodynamic diameter measurements depend on both the shape, the density and the orientation of the particles with respect to its direction of motion (Schinwald et al., 2012). Furthermore, the APS results suggested that the addition of 2.5 wt% functionalized rGO in the polymer matrix resulted in a decrease in the average particle size compared to the particles released from the neat PA6. Recent studies have shown that the addition of GRMs at concentrations as low as 0.5 wt % could significantly improve the mechanical properties of polymer composites (Netkueakul et al., 2020; Zeng et al., 2015). The presented PA6-rGO composites demonstrated improved mechanical properties as confirmed by the increased Young's modulus and tensile strength, compared to other GRM-PA6 and neat PA6 composites (Gomez et al., 2020). This increase in toughness could make the composites more challenging to crack, leading to the generation of smaller particles, as shown in the PA6-rGO. In contrast, the lower hardness of neat PA6 resulted in separation of larger sized particles (Zok and Miserez, 2007). In addition, a larger number of particles was collected from PA6-rGO composite samples than from the neat PA6 samples. This could be explained by the observed electrostatic charging in the neat PA6 particles during abrasion and their scattering, prior to their collection by the vacuum probe. Jian et al. reported that the electrostatic potential and the tribological behavior of PA6 during a wear process is not a simple mechanism and can be affected by internal phenomena, such as heat friction accumulation, physical adsorption, wear rate, and surface, as well as external conditions (Jian et al., 2009). Even though the underlying mechanisms were not defined, the electrostatic charging due to the abrasion and the subsequent heat production was observed in the neat PA6 particles, resulting in lower particle concentration. Focusing on the SMPS results only background signal was observed up to ~400 nm, which was followed by an increase in particles concentration at approximately 700 nm (detection limit of the instrument), indicating the existence of particles in larger dimensions, in accordance with the APS results (SI 7).

4.2. Detection of endotoxin content in PA6, PA6-rGO and rGO

An important aspect that needs to be evaluated before any biological assessment of a (nano)biomaterial is the possible contamination by endotoxins. It has been shown that endotoxin contamination of carbon-based nanomaterials may generate artifacts, which could distort biological outcomes, when investigating effects on immune-competent cells (Li and Boraschi, 2016). According to the chromogenic endotoxin assay, the endotoxin content in the tested materials was negligible (below 0.10 EU/mL). Since it has been reported that GRMs may interfere with traditional endotoxin assays, we further evaluated endotoxin, using the tumor necrosis factor-α (TNF-α) expression test (TET) (Mukherjee et al., 2016). As shown in SI 8, none of the materials (PA6, PA6-rGO and rGO) triggered tumor necrosis factor alpha (TNF-α) secretion in human monocyte-derived macrophages (HDMD) in the presence or absence of the specific lipopolysaccharide (LPS) inhibitor, polymyxin B, indicating that our tested materials were endotoxin-free.

4.3. Qualitative detection of rGO released from the PA6 matrix

It has been shown that fillers such as GRMs may be released from the polymer composite matrix as a result of the matrix degradation (*e.g.,* thermal degradation, hydrolysis, UV exposure), during the routine use of GRM enriched composites (Duncan and Pillai, 2015; Froggett et al., 2014). The released particles can either be GRMs fully embedded, partially protruding, or completely released (free-standing) from the polymer matrix. Hence, depending on their aerodynamic size and shape, they may pose a threat to human health.

Previous studies have shown that the release of fillers from polymer composites could be related to intrinsic failure mechanism. Release of rGO either as protruding or as free-standing from the PA6-rGO composite, during the abrasion process, could be explained by an interfacial debonding between the rGO and PA6 molecules or an adhesive failure as a result of the weak interaction between the rGO and PA6 matrix, as reported by previous studies (Massaq et al., 2019; Zaman et al., 2012; Zheng et al., 2019; Netkueakul et al., 2020). In addition, failure of graphene sheets is also highly possible, *i.e.,* graphene layer breakage. The failure mechanism of PA6-rGO composites can be examined by visualizing the surface of fractured composites by SEM imaging (Zaman et al., 2012). The fractured surface of PA6-rGO composites showed rougher structure and deeper cracks compared to that of neat PA6, since the incorporation of rGO could affect the crack propagation of the PA6 composite (SI 9a). Moreover, the characteristic layered and platelet-like structure of rGO was observed as it is released from the PA6 matrix, due to the adhesion failure between rGO and the matrix. Indeed, the exposed rGOs suggested a weak interaction between the rGO and the PA6 matrix, which could also be implied when the composites undergo an abrasion process. In addition, high-resolution TEM analysis of the abraded particles from PA6-rGO composites revealed the layered structure of rGO, appearing as protruding part from the PA6 matrix (SI 9b), thus confirming that rGO can be released from the polymer during the abrasion process. It is worth mentioning, that this layered structure can only be observed when rGO is wrinkled or when observed from the side of the stacked layers. Although we observed signs of possible rGO release, it was not possible to draw conclusions on the quantity of rGO released from the polymer. Considering the low percentage of rGO (2.5%) in the PA6 composite and the sensitivity of PA6 polymer even in mild acid conditions, it is technically very complex/impossible to determine the amount of rGO that would be present at the surface of the abraded particles of PA6-rGO or totally released from the polymer matrix.

4.4. Impact on lung cells in vitro

Numerous studies have proven that among the different routes of engineered nanomaterial (NM) exposure, the pulmonary exposure and consequently the respiratory tract is of the highest concern (Wang et al., 2015a, 2015b; Oberdörster et al., 2005, 2009). Once inhaled, carbon-based materials can reach the deepest regions of the respiratory tract (alveolar region) where they can accumulate for months and distribute to other organs (Li et al., 2013; Mercer et al., 2013). Upon inhalation, respirable particles deposit mainly in the alveolar lung region (Oberdörster et al., 2005; Rodrigues et al., 2020). Potential effects were therefore evaluated in this part of the respiratory tract, using the A549 cell line (human adenocarcinoma derived-alveolar epithelial type II cells), which is the most commonly applied cell culture model of human alveolar lung epithelium for hazard assessment. In most studies A549 cells are grown in 2D conformation and submerged in cell culture medium, which is not representative of the conditions in the human lung. However, when growing on permeable supports, A549 cells are able to form a polarized tight monolayer and can be maintained at

air-liquid interface (ALI) conditions, comparatively resembling native alveolar epithelia (Wu et al., 2018a 2018b; Chortarea et al., 2019). In addition, when cultured 24 h at ALI conditions, A549 cells actively secrete surfactant proteins, resulting in a surface tension similar to values measured *in vivo*, in pulmonary alveoli (Blank et al., 2006; Chortarea et al., 2015). Taking into consideration these important features, A549 cells were selected to assess the biological effects of pristine rGO, abraded PA6 and PA6-rGO composite materials on the alveolar epithelium. Material exposures were performed using a pseudo-ALI approach (where a thin layer of material suspension is applied apically on the insert), without disturbing the surfactant production. Furthermore, pseudo-ALI exposures are more relevant than fully submerged conditions since they result in faster particle deposition, lower particle agglomeration, and higher particle-cell interactions (Chortarea et al., 2019; Barosova et al., 2018; Endes et al., 2014).

An important consideration when performing safety assessment studies is the use of realistic exposure concentrations. In case of GRMs, human realistic exposure concentrations can only be estimated from the

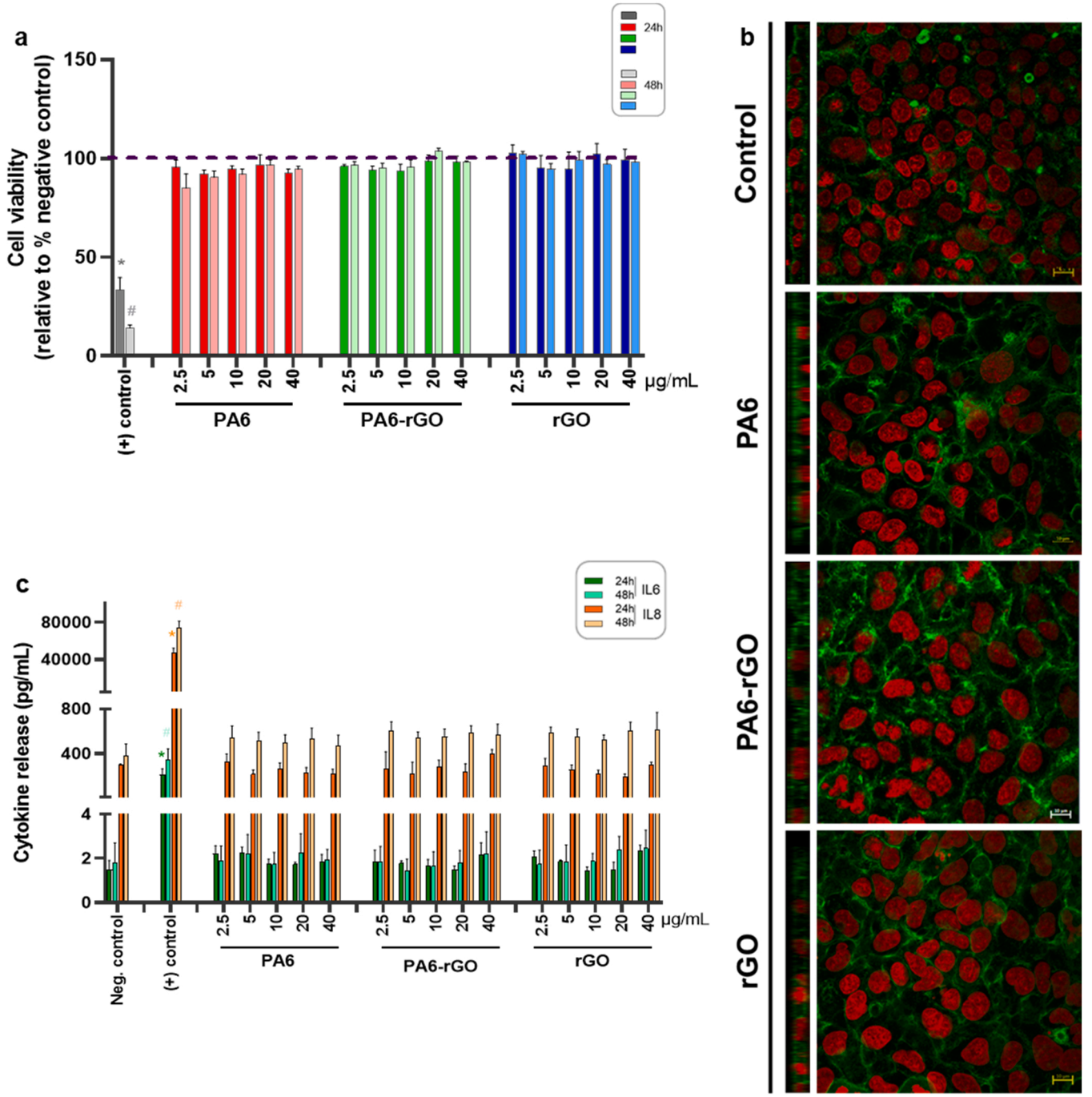

Fig. 3. (a) Cell viability of A549 epithelial cells, measured by the MTS assay after 24 h and 48 h treatment with rGO and the abraded particles from neat PA6 and PA6-rGO composites. 1000 µM $CdSO_4$ was used as a positive control. (b) Confocal LSM images of A549 cells after exposure to the tested materials (scale bars: 10 µm). The green color shows F-actin (cytoskeleton), red color shows DNA (cell nuclei). (c) Pro-inflammatory response of A549 epithelial cells after treatment with the tested materials. Concentrations of IL-6 and IL-8 were measured after 24 h and 48 h of materials exposure. One µg/mL TNF-α was used as the positive control. The results are shown as mean ± standard error of the mean (SEM) from at least three independent experiments. * indicates statistical significance compared to the negative control at 24 h of exposure ($p < 0.05$). # shows a statistically significant response ($p < 0.05$) at 48 h of material exposure.

existing limits for CNT pulmonary exposure, where a full working lifetime exposure would result in an alveolar mass retention of 10–50 μg/cm^2 and an acute lung exposure (24–48 h) would be in the range of 1 μg/cm^2 (Gangwal et al., 2011; Chortarea et al., 2017). The tested doses (2.5–40 μg/mL) in the present study correspond to 1.3–44 μg/cm^2 in the different plate formats used for the different cell types and therefore cover the human realistic doses (from low (2.5 μg/mL) to slightly overload (40 μg/mL) doses). The selected dose-range is based on human inhalation exposures as it is considered the primary and riskiest exposure route for nanomaterials. Considering other exposure routes (*e.g.* dermal, ingestion exposure) no human exposure data are available. For that reason and for comparability purposes, the same dose range was applied in the different biological systems under investigation.

To determine the acute impact (24 h and 48 h post-exposure) of the materials under investigation on the alveolar cells, cell viability, alterations in morphology and induction of pro-inflammatory reactions were evaluated, at different concentrations of materials (2.5–40 μg/mL). Adverse effects of particles released from the abrasion wheel on the cell culture models were not anticipated as the quantified amount of released particles was negligible. Moreover, no effects were noted in previous studies using a similar experimental setup (Netkueakul et al., 2020; Schlagenhauf et al., 2015).

Acute 24 h exposures to either pristine rGO or abraded PA6 and PA6-rGO composite particles did not significantly alter the mitochondrial activity of alveolar epithelial cells at pseudo-ALI conditions, as shown by the MTS viability results (Fig. 3a). Similarly, no reduction in cell viability was detected in the alveolar barrier, following 48 h exposure to the tested materials. In accordance with the viability results, no signs of morphological alterations were observed in cells exposed to the highest concentration of abraded particles and rGO (40 μg/mL) for 48 h, when compared to the negative control cultures (Fig. 3b). Importantly, the alveolar epithelial cell layer was maintained, without ruptures or signs of apoptosis (*i.e.*, fragmented cell nuclei or cellular blebbing) to the nuclei and cytoskeleton.

Analysis of interleukin-8 (IL-8), a critical airway epithelial-derived pro-inflammatory chemokine primarily implicated in acute inflammation and accumulation of neutrophils in inflammatory diseases, revealed that both abraded materials did not induce any effect on IL-8 secreted levels even after 48 h of exposure (Fig. 3c) (Mukaida, 2003). In addition, interleukin-6 (IL-6) a key inflammatory marker (in both acute and chronic inflammation) pivotal for the pathogenesis and exacerbation of numerous pulmonary diseases was evaluated (Rincon and Irvin, 2012). Exposure to different concentrations of abraded PA6 and PA6-rGO composite materials for up to 48 h did not elicit an increase in IL-6 levels compared to untreated cultures. Since IL-6 and IL-8 are fundamental for the initiation and activation of pivotal inflammatory pathways, evaluation of the secretion of these cytokines provides a valid indication of possible pro-inflammatory reactions. The absence of significant pro-inflammatory responses is in agreement with Wohlleben et al. who did not observe any significant toxicity in lung tissue exposed to polyurethane/3% CNT composites (Wohlleben et al., 2013). Consistent with our results, Irfan et al., demonstrated that dust particles released from silicon-PA6 composites and neat PA6 composites after a crash and drilling process, did not exhibit significant cytotoxicity following 48 h of submerged exposure in non-polarized A549 cells (Irfan et al., 2013). Similar observations were also reported in another study where no signs of acute adverse effects (*e.g.,* reduction in mitochondrial activity, or increased secretion of pro-inflammatory mediators) were detected in A549 cells, from neat epoxy or from the addition of CNTs (1%) to the epoxy matrix (Schlagenhauf et al., 2015).

The reliability and sensitivity of the pseudo-ALI A549 model was validated using crystalline quartz (DQ). DQ is a well-known inflammogenic material, classified as a group 1 human carcinogen (Wilbourn et al., 1997; Clouter et al., 2001; Monteiller et al., 2007). Several studies reported significant inflammatory effects both *in vitro* and *in vivo* after DQ administration (Chortarea et al., 2015, 2017; Barosova et al., 2020; Nakano-Narusawa et al., 2020; Beyeler et al., 2018; Endes et al., 2014). Hence, it is frequently used as a positive control for inflammatory responses in hazard assessment studies. As shown in SI 10, 24 h exposure to DQ (100 μg/mL) elicited significant release of both IL-6 and IL-8 in A549 cells, thus further confirming the responsiveness of the A549 cells under the specific culture and exposure conditions.

Similar to the abrasion materials, rGO-exposed A549 cells for 24 h and 48 h did not show evidence of increased pro-inflammatory response, neither in IL-8 nor in IL-6 secretion (Fig. 3c). On the contrary, Reshma et al., demonstrated that rGO treatment for 24 h resulted in a dose-dependent reduction in cell viability and NF-κB mediated inflammatory response in A549 2D cultures (Reshma et al., 2016). Dose-dependent toxicity in rGO exposed BEAS-2B (bronchial epithelial) and A549 (alveolar epithelial) cells was also noted by Mittal et al. (2016) These differences in biological response could be ascribed to differences in the physicochemical properties of the tested materials as well as differences in cell culture conditions and pseudo-ALI *versus* submerged conditions.

4.5. Impact on gastrointestinal cells in vitro

Another important exposure route for NMs is through the GI tract, where NMs can either directly be ingested or indirectly enter the GI tract by oral breathing and during the clearance process of formerly inhaled airborne NMs (Sohal et al., 2018). In contrast to large number of studies focusing on GRM inhalation, the impact of GRMs on the GI system has been largely overlooked, despite the potential implications on human health in both consumer and occupational settings (Pietroiusti et al., 2017). Caco-2 cells, a human colon adenocarcinoma-derived cell line, is the gold-standard for *in vitro* studies of the human intestinal epithelium, with wide-spread application in pharmaceutical and toxicological research (Kucki et al., 2016, 2017). The existing *in vitro* studies have predominantly been performed with non-polarized undifferentiated Caco-2 cells (representing pre-enterocytes) for fast and high-throughput screening of potential substances. Nevertheless, differentiated Caco-2 cells (21 days cultivation on microporous inserts) represent a more reliable model to mimic the small intestine's enterocyte barrier as they more realistically reflect the mature human enterocytes, both morphologically and functionally (*e.g.,* tight and polarized enterocyte-like epithelial cell layers with brush border and tight junction formation) (Kucki et al., 2017; Domenech et al., 2020; Carr et al., 2012). Therefore, a toxicological assessment of pristine rGO and abraded PA6 and PA6-rGO, using pseudo-ALI approach to induce the physiologically relevant, fully differentiated Caco-2 cells *in vitro* model of the human small intestinal epithelial barrier was performed.

To evaluate the effects of the tested materials on the intestinal cell viability, the mitochondrial activity was assessed after exposure to material concentrations ranging from 0 to 40 μg/mL for 24 h and 48 h. As shown in Fig. 4a, the enterocyte epithelial barrier initially demonstrated high resistance to abraded PA6 and PA6-rGO, as well as, to pristine rGO cytotoxicity. More specifically, cell viability at 24 h was unchanged, without significant reduction of mitochondrial activity, regardless of materials or concentrations tested. At the 48 h time-point, PA6-treated cells remained unaffected, while a slight reduction of viability was reported in PA6-rGO cultures at high concentrations (non-significant $p > 0.05$, 20 μg/mL; 77% viability, 40 μg/mL; 79% viable cells). For rGO, the decline in cell viability was more pronounced even at lower material concentrations (10 μg/mL; 72% viability, significant $p < 0.05$, 82% and 66% viability at 20 and 40 μg/mL respectively, non-significant $p > 0.05$) at 48 h. As only a few reports are available on the effects of GRMs on human enterocytes *in vitro*, and none of the existing studies have investigated the effects of rGO or GRM-embedded composite materials, a comparison with our *in vitro* intestinal results was limited. Nevertheless, the lack of acute effects on mitochondrial activity even at high concentrations (up to 80 μg/mL) was noted by Kucki et al. who investigated the toxicological impact of four types of GOs on

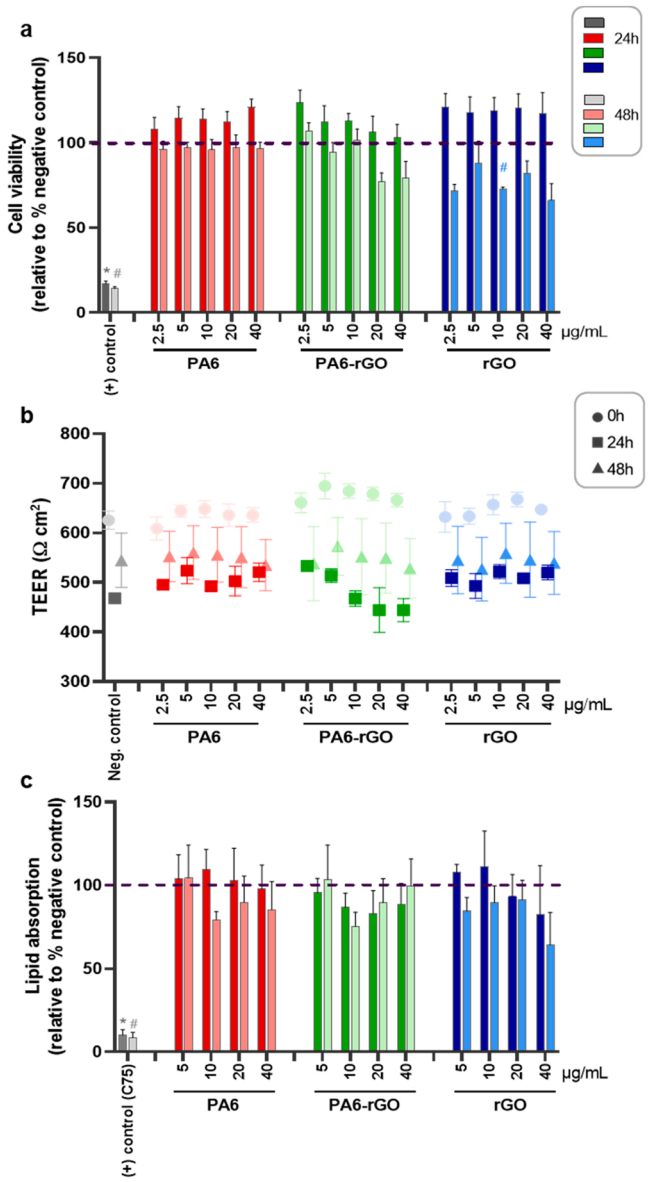

Fig. 4. (a) Impact of abraded particles (PA6, PA6-rGO) and rGO on cell viability of differentiated CaCo-2 intestinal epithelial cells after 24 h and 48 h of exposure (MTS assay). $CdSO_4$ served as a chemical positive control. (b) Assessment of the barrier integrity by TEER measurement before and after exposure to the tested materials (c) Lipid absorption was determined following 24 h and 48 h of exposure to the tested materials. Treatment of cells with the fatty acid synthase inhibitor C75 (50 μg/mL) for 24 h served as a chemical positive control for the investigation of lipid uptake. The results are shown as mean ± SEM from at least three independent experiments. * indicates statistical significance compared to the negative control at 24 h of exposure ($p < 0.05$). # shows a statistically significant response ($p < 0.05$) at 48 h of material exposure.

undifferentiated Caco-2 cells for 48 h (Kucki et al., 2016). Similarly, the viability of undifferentiated Caco-2 cells remained unaffected, following exposure to GO and few layer graphene (FLG) repeatedly for 4 days (Guarnieri et al., 2018). It is pertinent to note that previous studies reported that NM and, in particular, GRM uptake is significantly lower in differentiated Caco-2 barrier models compared to undifferentiated cells due to the lack of typical structures (*e.g.,* microvilli and tight junctions), which hinder NM internalization (Kucki et al., 2017; Guarnieri et al., 2018; Song et al., 2015). Hence, despite higher internalization, no acute toxicity GRM effects were noted in the existing studies.

To evaluate the functional integrity of the intestinal barrier, the transepithelial electrical resistance (TEER) values before and after material exposure were measured. No significant TEER reduction was reported when differentiated Caco-2 cells, were exposed to abraded PA6 or PA6-rGO even after 48 h of exposure (Fig. 4b). Similarly, no effect on barrier integrity was observed following exposure to pristine rGO, suggesting that the observed loss in mitochondrial activity did not have any impact on the barrier function. Consistent with our results, Domenech et al. found that neither GO nor graphene nanoplatelets (GNP) exposures were able to affect the functional/structural integrity of an intestinal co-culture barrier model (Caco-2/HT-29 cells), as reported by TEER and permeability measurements (Domenech et al., 2020). In addition, membrane integrity of cells was maintained even after treatment with digested GOs in a Caco-2 undifferentiated monolayer and a triple co-culture (Caco-2/HT-29/Raji) intestinal model (Guarnieri et al., 2018; Bitounis et al., 2020).

The lipid absorption at the brush borders of the enterocytes is a fundamental physiological function of the intestinal barrier (Hansen et al., 2007). To investigate possible alterations in the fatty acid uptake of differentiated Caco-2 cells after treatment with abraded composite materials and rGO, a lipid uptake assay was performed. Cell treatment with fatty acid synthase inhibitor C75 resulted in a significant decrease in lipid uptake at both 24 h and 48 h (Fig. 4c), suggesting a major defect in lipid absorption, in agreement with the observations of Hempt et al., and Accioly et al. Hempt et al. (2020); Accioly et al. (2008) On the contrary, no significant changes in fatty acid absorption were detected after treatment with abraded PA6, PA6-rGO and pristine rGO for 24 h. At 48 h of treatment with abraded PA6 and PA6-rGO a significant reduction was only observed at the concentration of 10 μg/mL (79% and 75% respectively, $p < 0.05$), however the higher material concentrations did not induce any evident effect in lipid uptake. In the case of rGO, a notable loss of fatty acid uptake was shown at the highest concentration tested, following 48 h of exposure (40 μg/mL; 64%, $p > 0.05$). It should be emphasized that no previous studies have analyzed possible alterations in the lipid absorption function of the intestinal barrier after GRM or other carbon-based material exposure. Interestingly, a previous study using synthetic amorphous silica did not observe any decline in the lipid uptake in a triple intestinal culture (Caco-2/HT-29/Raji co-culture) after 48 h of exposure (Hempt et al., 2020).

4.6. Impact on skin cells in vitro

The skin as the largest organ in the human body, with primary functions to defend and maintain physiological conditions, is considered one of the most common routes for GRM exposure, during the life cycle of GRM containing products (Pelin et al., 2018; Zhang et al., 2014; Pelin et al., 2018). Epidermal cells consist mainly of keratinocytes, structurally involved in maintaining the barrier function of the epidermis, but also exerting a key role in the initiation and perpetuation of skin inflammatory and immunological responses at the skin level (Hänel et al., 2013). Therefore, the potential dermatoxic effects of abraded rGO-composite materials and pristine rGO were investigated on human HaCaT skin keratinocytes, a non-tumorigenic, spontaneously immortalized human keratinocyte cell line, already employed to study skin toxicity of pristine GRMs (Frontiñán-Rubio et al., 2018; Pelin et al., 2017, 2020).

Initially, the acute effects on cell viability were evaluated by means of mitochondrial activity of HaCaT cells after two exposure times (24 h and 48 h) by the MTS assay (Fig. 5a). The pristine rGO induced a significant reduction of cell viability only after 48 h exposure to the highest concentration (40 μg/mL; 78% cell viability, $p < 0.05$), in line with the weak cytotoxic effects induced by other pristine GRMs such as FLG and GO on the same cell type (Pelin et al., 2017). However, treatment of keratinocytes with abraded particles from neat or rGO-reinforced PA6 composites did not induce any decrease in mitochondrial activity. In contrast, a slight increase on cell viability was observed after 24 h

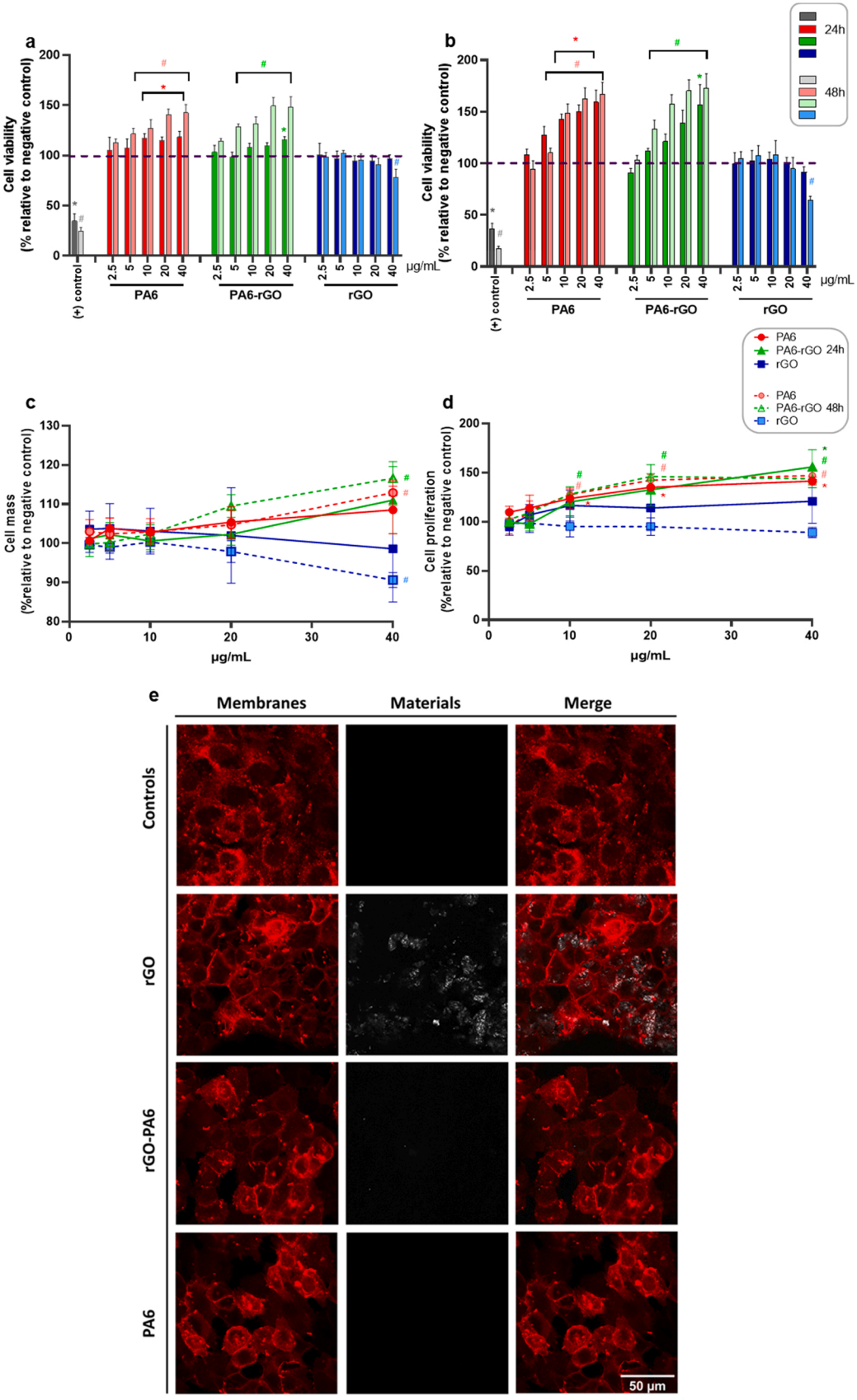

Fig. 5. Effect of rGO and abraded PA6 and PA6-rGO on the mitochondrial activity of HaCaT cells evaluated by (a) the MTS assay and (b) the WST-8 assay. Potential effects of the tested materials on skin cell proliferation assessed by (c) the SRB incorporation assay and (d) the BrdU assay. Data are the mean ± SEM of 3 independent experiments. * indicates statistical significance compared to the negative control at 24 h of exposure ($p < 0.05$). # shows a statistically significant response ($p < 0.05$) at 48 h of material exposure. (e) Confocal micrographs of HaCaT cells exposed to 40 µg/mL of rGO, abraded PA6-rGO and abraded neat PA6 for 48 h. Plasma membrane of HaCaT cells was labeled with the fluorescence DiL dye (red, left panel). rGO is visualized by reflection mode acquisition (white, middle panel); confocal reconstruction of red DiL labeled HaCaT cells merged with white reflecting rGO (merged images, right panel). Original magnification: 60×. Scale bar: 50 µm.

exposure, which was more pronounced after 48 h exposure (significant from the concentration of 5 μg/mL, $p < 0.01$). In particular, after 48 h, abraded PA6 and PA6-rGO particles increased cell viability at 143% and 148%, respectively, at the highest concentration. To further validate the results from the MTS assay, the WST-8 assay was also performed, as a widely used assay to evaluate the mitochondrial damage caused by different GRMs on a wide range of *in vitro* models, including HaCaT keratinocytes (Pelin et al., 2020, 2017; Chang et al., 2011; Wang et al., 2014). WST-8 confirmed the results obtained by the MTS, although more substantial effects were reported (Fig. 5b). More specifically, rGO induced a significant reduction of cell viability after 48 h exposure to the highest rGO concentration (40 μg/mL; 64% cell viability, $p < 0.001$). Moreover, as observed with the MTS assay, abraded PA6 and PA6-rGO particles significantly increased cell viability, already after 24 h exposure and starting from the concentration of 10 μg/mL (142% cell viability, $p < 0.05$) for PA6 and at the highest concentration of 40 μg/mL PA6-rGO (156% cell viability, $p < 0.05$). The effect was more pronounced after 48 h exposure, being significant starting from the concentration of 5 μg/mL ($p < 0.05$), inducing a maximum increase of 167% and 173% for abraded PA6 and PA6-rGO particles, respectively, at the highest concentration. To quantify the viable attached cells, without relying on metabolic activity measurements that might lead to false positive overestimation of cell viability, the cell mass was determined using the well-established SRB assay (Skehan et al., 1990). A similar trend to the mitochondrial activity assays was observed. Pristine rGO resulted in a slight but significant reduction of cell mass at 40 μg/mL (90%, $p < 0.05$), while abraded composite particles significantly increased cell mass (113%, $p < 0.05$%, and 117%, $p < 0.05$, for PA6 and PA6-rGO, respectively) at the same concentration, and after 48 h of exposure (Fig. 5c). To further investigate whether abraded PA6 can promote cell proliferation, the % of proliferating cells was determined as shown in Fig. 5d. No alteration of cell proliferation was induced by exposure to pristine rGO for neither 24 h nor 48 h. On the contrary, abraded PA6-rGO and PA6 increased cell proliferation already after 24 h at the highest concentrations ($p < 0.05$). At 48 h of exposure to abraded composites, cell proliferation was more evident, being significant already at the concentration of 10 μg/mL and inducing maximum effects of 147% and 144% for abraded PA6 and PA6-rGO, respectively ($p < 0.05$). These results suggest that: *i*) the increased cell viability induced by abraded PA6 and PA6-rGO may be dependent on a proliferative stimulus and *ii*) the proliferative stimulus seems to be exerted by abraded PA6. Indeed, Dias et al. recently reported the ability of PA6 to promote cell proliferation in murine fibroblasts when employed as a nanostructured scaffold, indicating its potential of modulating skin regeneration and wound healing parameters at cellular and histological levels (Dias et al., 2019). This phenomenon may be explained by the structural similarities between PA6 and proteins. Indeed, the amide groups of the polymer can interact by hydrogen bonds with cellular molecules, providing a structural environment able to improve cell growth (Dias et al., 2019). In addition, cell proliferation may be promoted and sustained by the hydrophilic wetting behavior of PA6 (Krysiak et al., 2020).

Possible alterations in cell morphology were visualized by confocal microscopy after staining plasma membranes of HaCaT cells with the DiL fluorescence dye. Negative control cultures displayed the typical cobblestone morphology of skin keratinocytes, which was slightly condensed in cells treated with 40 μg/mL of each material for 48 h, particularly for rGO-treated cultures. Moreover, the morphology of rGO-treated cells showed a moderate cell shrinkage, in line with the observed cytotoxic effect.

Fusco et al. recently reported that keratinocytes are able to selectively sense and interact with GRMs at amounts as low as 1 μg/mL (Fusco et al., 2020). In addition, further analysis reported that GRM cytotoxic effects on HaCaT cells are only partially reversible, probably because of their ability to be internalized inside keratinocytes (Pelin et al., 2020). To investigate the interactions between the materials and epidermal cells, HaCaT cells exposed to pristine rGO, abraded PA6-rGO and PA6 (40 μg/mL) for 48 h were subjected to confocal microscopy analysis, in which materials were visualized in white exploiting their light reflection properties during the confocal acquisition. As shown in Fig. 5e, rGO and PA6-rGO were able to interact with cells, where the presence of rGO, and to a far less extent PA6-rGO, was visualized bound to the membranes and inside keratinocytes. In line with this observation, using reflection mode acquisition, different GRMs (*e.g.* GO, FLG) were captured to interact and penetrate the plasma membrane of HaCat cells (Pelin et al., 2017). Reflection mode, however did not allow the detection of the abraded PA6 polymer in the cells, due to low contrast of these particles. Similarly, the low signal given by PA6-rGO acquired in reflection mode by confocal microscopy analysis could be ascribed to a quenching effect by PA6 polymer bound to rGO. This hypothesis is supported by the lack of light reflection properties of PA6, which could partially mask the signal given by rGO.

4.7. Impact on immune cells in vitro

The immune system identifies and protects the body from infections and other exogenous materials. Therefore, understanding the interaction of GRMs with the pivotal cells of the innate immune system is of particular importance (Boraschi et al., 2017; Lin et al., 2021; Mukherjee et al., 2018; Russier et al., 2013). The key front-line cells of the immune system assigned to eliminate foreign materials and assist in tissue remodeling after injury across the whole body are macrophages (Mukherjee et al., 2017). In a pulmonary exposure scenario, macrophages will be the first immune cells interacting with GRMs and dealing with their clearance or long-term persistence (Schinwald et al., 2012; Rodrigues et al., 2020; Roberts et al., 2016; Bengtson et al., 2017). The effect of abraded particles and pristine rGO was therefore assessed in human macrophage differentiated THP-1 cells. The biological response was also tested in murine macrophage-like cells (RAW 264.7) to determine possible difference in the behavior of the tested materials towards human or murine cells. THP-1 and RAW 264.7 macrophage models act as proxy for either tissue-recruited macrophages upon inflammation signaling or tissue resident macrophages, such as alveolar macrophages in the lungs.

Cell viability of THP-1 differentiated and RAW 264.7 macrophages exposed to PA6, PA6-rGO and rGO was determined using the MTS assay. As seen in Fig. 6a-b, abraded PA6 and PA6-rGO did not decrease the mitochondrial activity of either THP-1 differentiated or RAW 264.7 macrophages even at the highest concentration (40 μg/mL). In agreement with our findings, Netkueakul et al. did not observe any significant cytotoxic effects of abraded particles from epoxy/1%GRM (GOs, rGO or GNPs) composites on THP-1 differentiated macrophages, at the same exposure concentrations (Netkueakul et al., 2020). In the same study, pristine GRMs, including rGO, did not reduce the cellular mitochondrial activity upon exposure to concentrations of up to 40 μg/mL. In addition, studies focusing on abraded polymer composites reinforced with other carbon-based materials, *i.e.,* CNTs, found that the abraded particles from epoxy/1%CNT composites did not cause acute effects on mitochondrial activity of THP-1 cells, while pure CNTs resulted in a significant decrease in cell viability (Schlagenhauf et al., 2015). In accordance with the above reported cell viability results in the skin and GI *in vitro* models, pristine rGO did induce a dose-dependent loss of cell viability in both macrophage cell lines (significant at concentrations of 20–40 μg/mL for THP-1 cells and 10–40 μg/mL for RAW 264.7 cells, respectively). Moreover, no induction of cytotoxic reactions was reported for RAW 264.7 macrophages after exposure to abraded materials, while a significant release of lactate dehydrogenase (LDH) was observed, following 24 h exposure to 20 and 40 μg/mL of pristine rGO, supporting the MTS data (SI 11). Consistent with our results a dose-dependent decline in cell viability, especially at higher rGO concentrations (from 20 μg/mL), has been observed in bone marrow derived macrophages as well as in the J774A.1 macrophage cell line (J. Wu et al., 2018; Y. Wu et al., 2018).

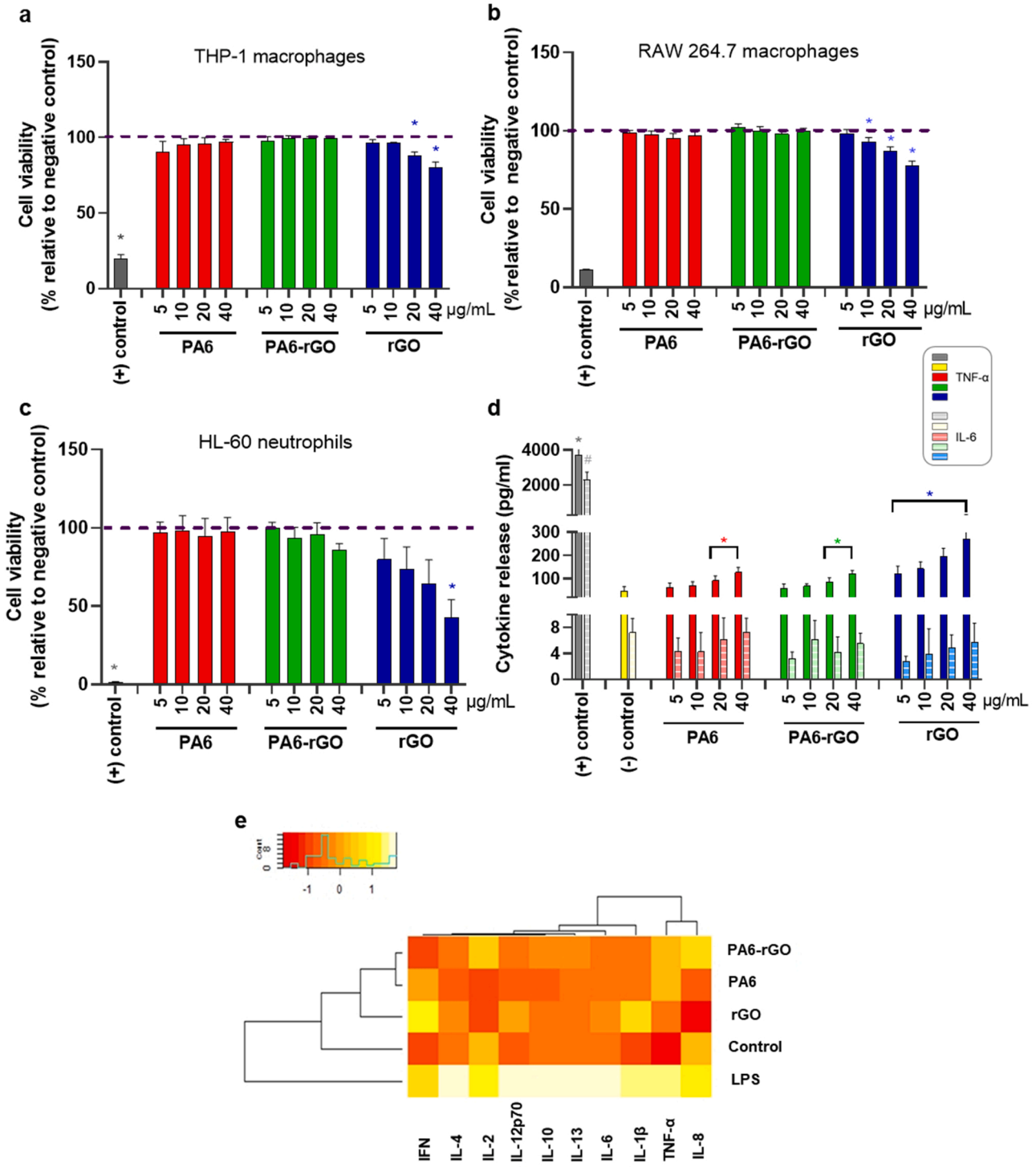

Fig. 6. Cell viability (MTS assay) of (a) THP-1 and (b) RAW 264.7 macrophages and (c) neutrophil-like HL-60 cells (ATP assay) exposed to increasing concentrations of rGO and abraded PA6 and PA6-rGO composites for 24 h. (d) Cytokine release by RAW264.7 macrophages. IL6 and TNF-α levels were determined after incubation with increasing concentrations of PA6, PA6-rGO and rGO. Cells exposed to 1 µg/mL LPS were used as positive control. Data are the mean ± SEM of 3 independent experiments. The * symbol represents $p < 0.05$ as compared to the negative control. (e) Cytokine profiling and hierarchical cluster analysis of inflammatory mediators released in differentiated THP-1 macrophages exposed to rGO, abraded PA6-rGO and PA6. Cells exposed to 0.1 µg/mL LPS were used as positive control. Each branch in the dendrograms shows the similarity between samples; the shorter the branch, the more similar the samples.

This stands in contrast with the work of Netkueakul et al. and Li et al. where no significant cytotoxicity was shown in rGO-treated THP-1 cells (Li et al., 2018; Netkueakul et al., 2020). Those differences in biological responses may depend on differences in the lateral dimensions, thickness and the amphiphilic properties of the materials.

Macrophages are also known to be involved in the initiation, progression, and resolution of inflammation (Zhou et al., 2012). Hence, to further evaluate the immunological impact of the tested materials in differentiated THP-1 cells, a multiplex-cytokine array analysis of ten crucial pro-inflammatory mediators was conducted at a sub-toxic concentration (20 µg/mL). In parallel, hierarchical clustering was carried out to draw associations between cytokine responses evidenced for

pristine rGO, the abraded PA6-rGO and PA-6, the LPS positive control, *versus* the negative control in human macrophages (Fig. 6e). The cytokine profiling analysis clearly demonstrated that the effects induced by the tested materials are distinctly different from the effects of LPS. Moreover, the cluster analysis suggested that the cytokines could be broadly separated into two main clusters: those affected by high secretion of cytokines generated by the LPS treatment and those affected by rGO, PA-6-rGO, and PA-6 treatment. More specifically, a significant increase in the secretion of interferon gamma (IFN-γ) was revealed in THP-1 cells when exposed to rGO and PA-6, comparable to the effect induced by the positive control LPS, a well-known stimulator for cytokine secretion in these cells. Moreover, two classical Th1 pro-inflammatory cytokines, TNF-α and interleukin-1beta (IL-1β), were significantly upregulated following acute exposure to all three materials (SI 12a), and IL-1β production was blocked by the pan-caspase inhibitor, zVAD-fmk and the selective NLRP3 inhibitor, MCC950 (SI 12b), suggesting that these materials triggered inflammasome activation, as shown for several other NMs (Sun et al., 2013). No significant release of IL-2, IL-4, IL-6, IL-8, IL-10, IL-12 and IL-13 was reported in material-treated THP-1 cells compared to the untreated cells. Similar to the results obtained with human macrophages, murine RAW 264.7 cells did not show significant upregulation of the crucial cytokine IL-6 regardless of the material applied, while significant TNF-α release was noted following exposure to all three materials (20 and 40 μg/mL for PA6 and PA6-rGO, all tested concentrations for rGO), as shown in Fig. 6d. Comparing THP1 and RAW 264.7 cells, no species-to-species variations in the investigated biological responses were observed, as similar effects were reported in both human and mouse cells.

Previous reports showed that neat polymer matrix materials such as epoxy did not trigger significant pro-inflammatory responses on immune cells (Netkueakul et al., 2020; Schlagenhauf et al., 2015). However, the present study demonstrated that abraded neat polymer PA6 did elicit significant release of three pivotal pro-inflammatory proteins in THP-1 cells. More specifically, upregulation of IFN-γ, a key player in host-defense against pathogens, might indicate that abraded particles from this polymer matrix may be recognized as intracellular parasites by THP-1 cells, leading to increased IFN-γ secretion. Moreover, both abraded materials (neat polymer PA6 and composite PA6-rGO) resulted in secretion of TNF-α and IL-1β cytokines that would typically lead to recruiting more immune cells *i.e.*, neutrophils, monocytes/macrophages to the affected areas, as a hallmark of acute inflammation (Ma et al., 2015). In addition to the endogenous inflammogenic potential of the polymer matrix, the potential inflammation of PA6-rGO could be explained by the transformation of rGO during the production process of the composite or due to protruding or released GRMs from the polymer matrix. However, the magnitude of the pro-inflammatory effect induced by the abraded PA6-rGO particles was notably lower compared to that induced by pristine rGO or the LPS control, suggesting only a minor pro-inflammatory response (SI 7b). Since the PA6-rGO composite material contains only a small percentage of rGO (2.5%), the observed limited toxicity of the composite material (containing a small % of rGO) compared to the pristine rGO is probably due to the low amount of rGO in the composite, the endogenous inflammogenicity of the neat polymer PA6, and not to a different mechanism of toxicity. Previous studies showed that GRM (particularly GO) treatment could provoke inflammatory responses, including the production of inflammatory cytokines by macrophages (Ma et al., 2015; Russier et al., 2013). The cytokine profiling experiments revealed that rGO triggered the cytokine production of the M1 markers TNF-α and IL-1β in THP-1 cells, suggesting possible inflammasome activation. These findings support those recently reported by Gurunathan et al. who observed significant stimulation of TNF-α and IL-1β secretion, following exposure to vanillin-functionalized rGO in THP-1 cells (Gurunathan et al., 2019). A similar trend was found for TNF-α secretion in primary and J774A.1 macrophages after treatment with two types of rGO (Wu et al., 2018a, 2018b).

To gain more insights into the interaction of the tested materials with macrophages, the cellular morphology was closely examined. Conventional light microscopy images of RAW 264.7 macrophages upon 24 h exposure to abraded PA6 and PA6-rGO materials revealed no signs of modification in cellular morphology even at the highest concentration of 40 μg/mL (SI 13). Correspondingly, no major alterations were observed in THP-1 cells after 24 h exposure to abraded GRM epoxy composites (Netkueakul et al., 2020). In the case of pristine rGO, although increased rGO accumulation was observed on the cells surface, the shape of the RAW264.7 macrophages was not affected at low concentrations (5–20 μg/mL). However, macrophages treated with 40 μg/mL of pristine rGO showed a rounder appearance compared to untreated control cells. In good agreement with our observations a loss of protrusions with a subsequent morphological shift towards rounded cells has been previously demonstrated after rGO exposure (20 μg/mL) in primary macrophages (Wu et al., 2018a, 2018b). The observed morphological alterations might indicate an increased rGO internalization by the macrophages. Moreover, the significant TNF-α secretion in RAW 264.7 cells could lead to the activation of macrophages into a pro-inflammatory state, which can lead to similar alterations in the cellular shape and could be a hint for the intrusion of rGO onto the plasma membrane, as shown by Wu et al. (2018a), (2018b) In support to that Li et al. demonstrated that while GO nanosheets are mostly associated with the surface membrane in THP-1 cells, rGO was principally internalized by phagocytosis (Li et al., 2018).

Several studies have shown that macrophages may be more susceptible than other cell types to the biological effects of particles, due to the greater dose of internalized particles. A previous study of a panel of metal oxide nanoparticles showed that the alveolar macrophage cell line was the most sensitive cell model among the 12 cell models tested (Farcal et al., 2015). The toxicity of metal/metal oxide particles may be explained by the rapid dissolution of the particles in the acidic environment of the lysosomes. In addition, high aspect ratio materials may cause lysosomal destabilization, and subsequently lead to pro-inflammatory cell activation. However, the materials tested here are not considered high aspect ratio materials as abraded particles and GRMs are not necessarily fiber-like and their biological effects depend on different material properties, not only the lateral dimensions (Wick et al., 2014). Nonetheless, the lateral dimensions of graphene oxide (GO) have been shown to play a role for interleukin-1β (IL-1β) and transforming growth factor-β1 (TGF-β1) production and a more recent study has confirmed that the lateral dimensions may impact on cellular uptake and subsequent biological effects in liver cells (Wang et al., 2015a, 2015b; Li et al., 2021).

Another important immune cell type often neglected in toxicological studies is neutrophils, the most abundant circulating leukocytes and among the first cells to be recruited in the airways, upon lung exposure to GRMs (Keshavan et al., 2019). These cells also play a key role in the initiation of inflammation in several tissues as well as in GRM biodegradation processes (Mukherjee et al., 2018a, 2018b; Kurapati et al., 2015). There is a paucity of data on the biological effect of GRMs on neutrophils and the few available studies mainly focused on the degradation of GRMs by a myeloperoxidase-dependent mechanism in neutrophils and not on immunotoxicity. Mukherjee et al. recently reported that GO sheets with differing lateral dimensions triggered a dose-dependent loss of mitochondrial activity in neutrophils as measured by the ATP assay. At the same time, GO acted directly on the neutrophil cell membrane, leading to cell activation (Mukherjee et al., 2018b). Therefore, it is important to know if pristine rGO and abraded particles from rGO-reinforced composite materials have an impact on neutrophils. Focusing on neutrophils, cell viability was determined on differentiated HL-60 cells using the ATP assay, as the MTS assay was not appropriate for this non-adherent cell line (data not shown). Consistent with the macrophage viability results, no significant effect on the viability of PA6 or PA6-rGO exposed HL-60 cells was observed (Fig. 6c), but a 24 h rGO treatment revealed a dose-dependent loss of

mitochondrial activity, only significant at the highest concentration (40 μg/mL, 50% viability). In addition to the viability assay, a cytokine array was performed in neutrophils to examine possible induction of pro-inflammatory processes (SI 14). In contrast to THP-1 cells, cluster analysis in exposed HL-60 cells revealed a large single cluster with low cytokine secretion for all tested cytokines, suggesting that neutrophils might not be a good model for cytokine screening. Furthermore, in HL-60 cells, no distinct cytokine upregulation was reported, except for LPS-treated cells (SI 1).

An important, non-trivial matter in relation to the *in vitro* results obtained with respect to pristine rGO, abraded neat PA6 or rGO-reinforced PA6 is the *in vitro* dosimetry. It has been shown that cellular uptake of gold nanoparticles depends on their sedimentation and diffusion velocities, while it is independent of size, shape, density, surface coating and the initial concentration of the nanoparticles (EC et al., 2011). More recent studies of so-called ''buoyant'' nanoparticles (*e.g.* polypropylene) have shown that their biological activities may be underestimated when using conventional submerged cell culture methods (CY et al., 2016). In the present study, A549 and Caco-2 cells were exposed using a more physiologically relevant (for the lung and the GI) pseudo-ALI approach, which allows faster particle sedimentation and more particle-cell interaction compared to the conventional submerged exposures. Regarding the skin (HaCaT) and immune (THP-1, RAW 264.7, and HL-60) cells, such pseudo-ALI exposures are not relevant; therefore, submerged exposures were applied. The existing models to estimate *in vitro* concentration of nanomaterials in submerged conditions (*e.g.* the *in vitro* sedimentation, diffusion, and dosimetry (ISDD) model, the distorted grid (DG) model, or the 3D-sedimentation-diffusion-dosimetry (3DSDD) model) were developed and are suitable only for spherical particles, such as spherical silica, gold, and metal oxide nanoparticles. They have a limited applicability for non-spherical materials (*e.g.* GRMs and CNTs) due to their different form factor and heterogeneity (DeLoid et al., 2014, 2015; Böhmert et al., 2018). Consequently, determining the GRM cell delivered dose in submerged conditions is still a challenge due to the analytical difficulties of quantifying the GRM dose delivered to cells, as it would require several analytical techniques and cellular uptake quantification. Particularly, for the abraded PA6 and PA6-rGO materials, it would be almost impossible as the cellular internalisation cannot be visualised with the existing methodology *i.e.,* TEM, Raman microscopy or optical microscopy and LSM reflection mode (as we have shown for RAW 264.7 and HaCaT cells).

4.8. Pulmonary effects in mice

The *in vitro* investigations demonstrated that pristine rGO was the material of highest concern amongst the tested materials, and that the immune cells and in particular the macrophages were the most responsive *in vitro* models both with respect to abraded materials (neat PA6 and PA6-RGO) and pristine rGO. Amongst all exposure routes, inhalation is the most rapid route of entry into the body and the only route in which macrophages would interact immediately, and without any intervening barrier, with the materials, should these respirable materials reach the alveoli. Considering that macrophages and neutrophils along with epithelial cells are the key drivers of the pulmonary response to respirable materials reaching the alveoli, we sought to study whether the rGO results obtained *in vitro* would translate into a macrophage-driven inflammatory response in the lungs of mice. Based on the *in vitro* results, we anticipated that abraded (neat PA6 and PA6-rGO) materials would cause limited inflammation *in vivo* while the response to pristine rGO would be more pronounced but still moderate. Moreover, the comparative results obtained using epithelial A549 lung cells (negative) and THP-1/RAW264.7/HL-60 immune cells (positive) suggested that the pulmonary response to rGO would be mostly driven by the resident macrophages, but would not prevent the resolution of this inflammation with time.

After a single exposure to abraded PA6-rGO, histopathological analysis of lung sections did not reveal any alteration of the lung tissue at the tested time-points (Fig. 7a). Absence of obvious cell recruitment or tissue damages was also noted after exposure to the low dose of pristine rGO (rGO-0.3 μg), neat polymer alone (PA6) or vehicle control. In contrast, exposure to high dose of pristine rGO (rGO-15 μg) induced macrophage-driven granuloma-like formations at all considered time points, and a clear infiltration of immune cells at 1 and 7 days. Interestingly, the location of those inflammatory structures were overlapping with material accumulation sites. Such reactions to foreign materials occur when materials cannot be easily eliminated from the tissue (Williams and Williams, 1983; Anderson et al., 2008). The key component of granuloma-like formation is the fusion of numerous macrophages into multinucleated cells, which are able to phagocytose particles that can be larger than 10 μm (Anderson et al., 2008). Noteworthely, the pronounced inflammatory structure formation observed at day 1 and 7 was followed by an obvious tissue recovery by day 28 (*i.e.*, with notable reduction in granuloma size, Fig. 7a). These results are not consistent with the findings of a previous study in which a prolonged inflammation over 90 day after exposure was associated to the presence of large, black and compact rGO agglomerates that persisted in lung tissue for up to 90 days without being phagocytosed (Bengtson et al., 2017). These results suggest that bio-persistence of materials was the leading cause for a prolonged inflammation, hence material clearence could in contrast be associated to inflammation resolution. In our study, the decrease in granuloma size and resolution of cell influx and inflammation over time is therefore likely to result from a successful rGO internalization and elimination by macrophages. Moroever, the *in vivo* pulmonary impact of rGO has been largely overlooked in comparison to other GRMs (Fadeel et al., 2018). In the few existing studies comparing GO and rGO, GO seemed to provoke more inflammogenic responses compared to rGO (Bengtson et al., 2017; Poulsen et al., 2021).

Adverse effects were also assessed by measuring total protein and LDH release to the airways. These two markers are typically used as hallmarks of lung epithelium tissue damage (Moalli et al., 1987). For the abraded PA6-rGO and PA6 materials, no significant variations of protein concentration or LDH activity in bronchoalveolar lavage (BAL) fluid were observed (Fig. 7b-7c), suggesting no disruption of the air-blood barrier and the lung epithelium, in agreement with the absence of responses found in the A549 cell model (Fig. 2). Despite the observation of granulomatus formation after exposure to high dose of rGO (rGO-15 μg), no significant ($p > 0.05$) effects on BAL proteins or LDH release were seen at 1, 7, or 28 days post-exposure, suggesting that the response to rGO was mostly driven by immune cells.

In BAL fluid, no variation in the total cell number was observed for any of the materials tested (Fig. 7d), but there was an increase in neutrophil numbers at day 1 after exposure to either abraded PA6-rGO or PA6 (Fig. 7e). Nevertheless, this neutrophil recruitment was not stastistically significant compared to the negative control. In contrast, a significant increase in neutrophils was found after exposure to rGO-15 μg, whereas no difference was observed for the lowest dose (rGO-0.3 μg) compared to the negative control. Interestingly, 7 days after exposure, an increase in eosinophils was found in the alveolar space of mice treated with either PA6-rGO ($p = 0.1217$) or rGO-15 μg ($p = 0.0543$). However, after 28 days, we did not detect any difference in eosinophils or neutrophils compared to the negative control for any of the materials tested. This suggested a recovery from the inflammatory stressor and is in agreement with the histological evaluation. Despite this recovery, the presence of multinucleated macrophages was still significant at 28 days for rGO-15 μg in comparison to the negative control or other conditions, suggesting that the higher amount of materials was delaying clearance and complete resolution.

To further characterize the lung inflammatory response, the concentration of 13 inflammatory mediators was evaluated in digested lungs at days 1, 7 and 28. As shown in Fig. 8, there was no significant change in any of the mediators tested, suggesting a low inflammatory

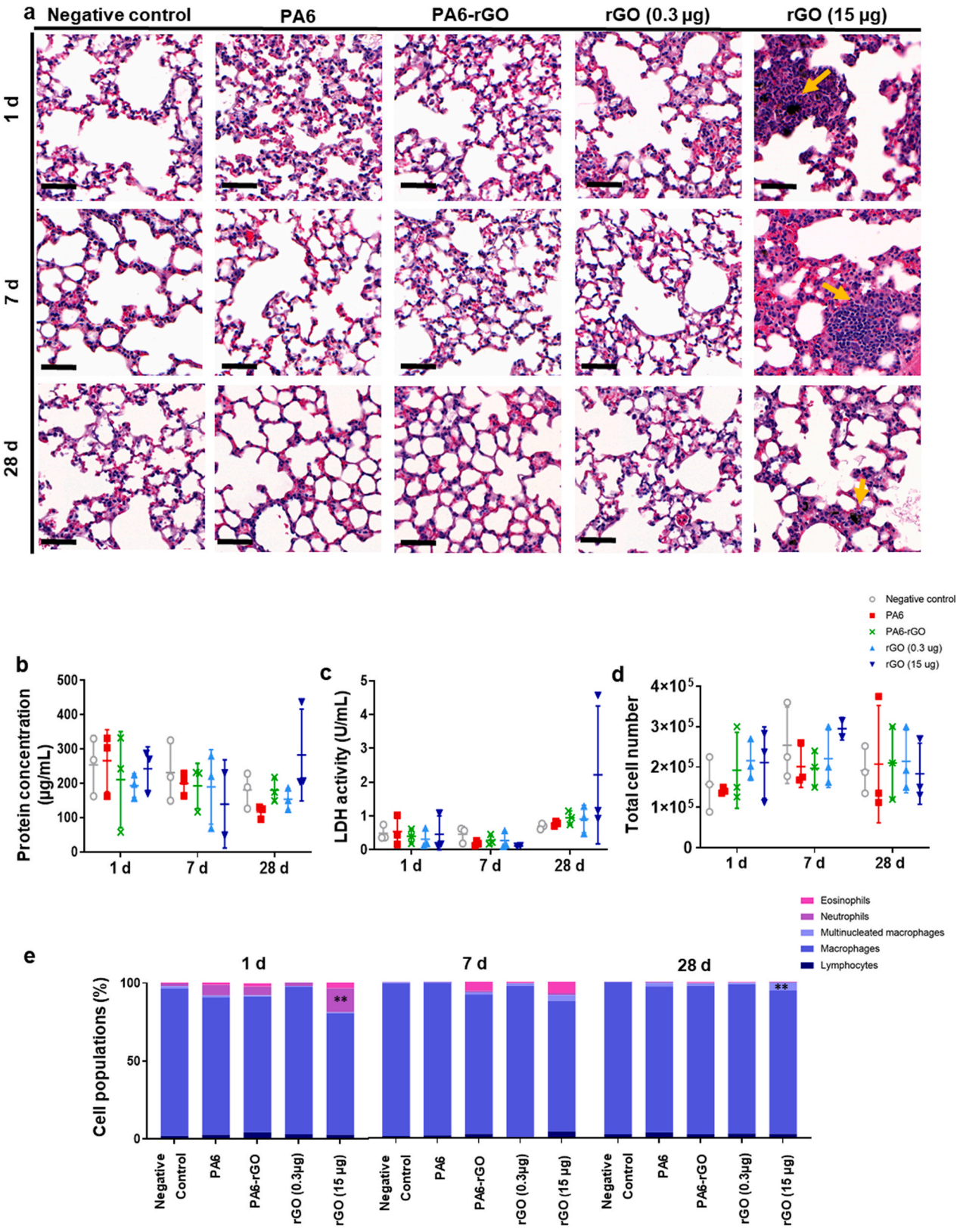

Fig. 7. Animals (n = 3) were exposed by oropharyngeal aspiration to abraded polymer (PA6, 15 µg), abraded composite (PA6-rGO, 15 µg; with 2.5% rGO, hence 0.375 µg of rGO in 15 µg of PA6-rGO), reduced graphene oxide (rGO, 0.3 µg or 15 µg; 2.5% of 15 µg equals to about 0.3 µg), or negative control (BSA 0.1% in water). (a) Representative images of H&E-stained lung sections from mice exposed to rGO and abraded composites, following 1, 7 and 28 days after oropharyngeal aspiration. Arrows indicate the formation of granulomas after treatment with rGO. (b) Protein concentration and (c) LDH activity in BAL fluid of exposed mice(d) Total cell number and (e) cell population (%) of BAL samples from mice after 1, 7 and 28 days following material administration. Data are presented as mean ± SD. The * symbol represents $p < 0.05$ as compared to the negative control.

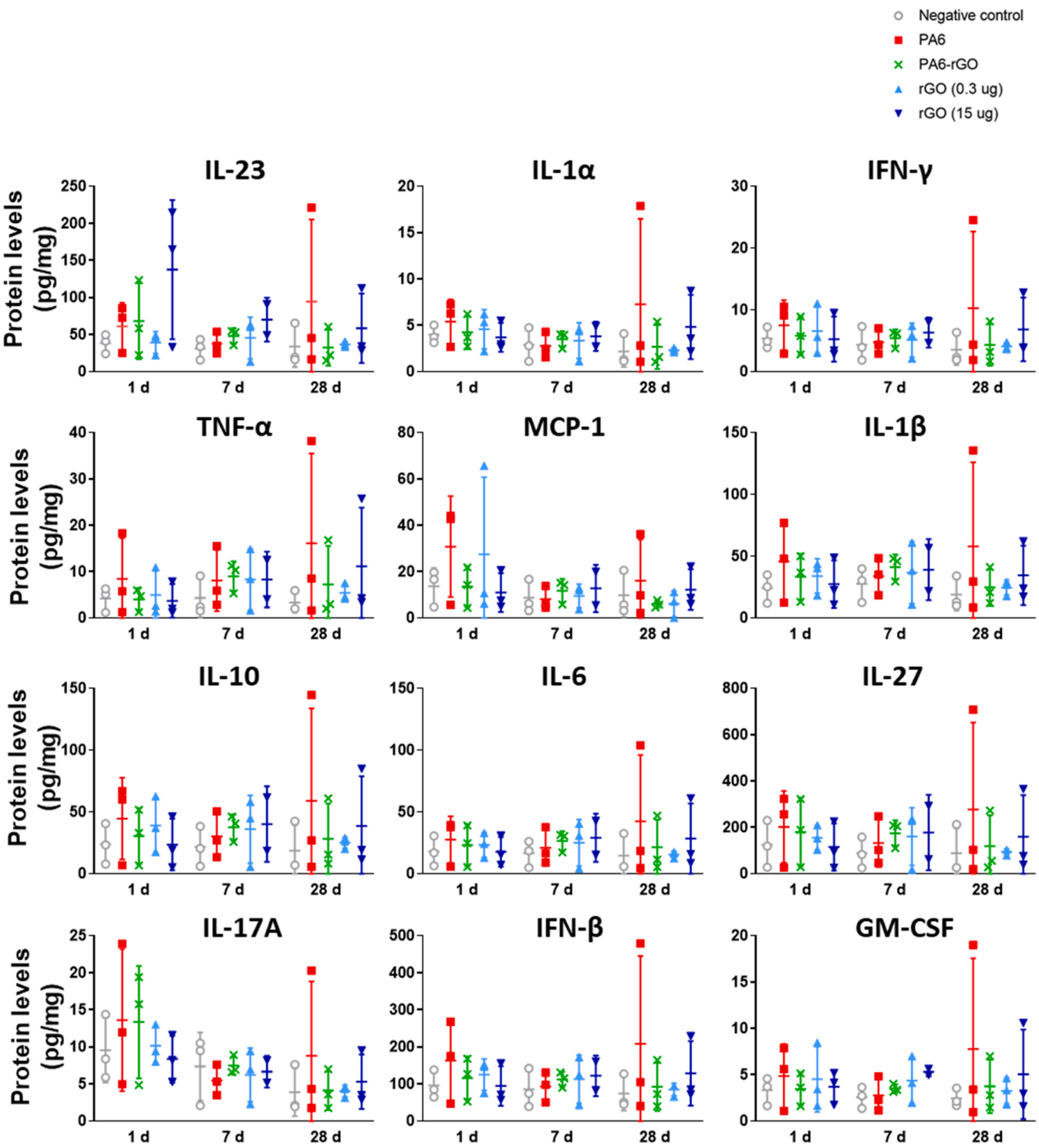

Fig. 8. Inflammatory response to rGO and abraded composite materials (neat PA6, PA6-rGO) in the lungs of mice after 1, 7 and 28 days. Individual data points corresponding to each animal are plotted alongside mean values. Data are presented as mean ± SD.

profile for all the materials tested. In addition, the concentration of TNF-α and IL-6 was assessed in the BAL fluid and found to be below the detection limit (7.8 pg/mL) of the assay (SI 16). Taken together, neither BAL fluid nor whole lung measurements showed significant cytokine secretion, which is in line with the moderate influx of immune cells in BAL fluids (PMNs, macrophages, or lymphocytes), irrespective of the materials considered (Fig. 7e).

It should be noted that the unaligned significant response observed for one animal (out of 3) for all tested cytokines (and total cell number) after exposure to abraded PA6 at 28 days (Figs. 7 and 8) was not anticipated. The discrepancy could not be attributed to technical or instrumental errors as the measurements were repeated and obtained the same results. In addition, the health and behaviour of this specific animal before the terminal procedure was not of concern (data not shown); hence, there was no valid reason for removing the animal from the study. The observed odd response should therefore be attributed to animal variability.

In summary, pulmonary exposure to abraded PA6-rGO in mice

induced a weak but not significant lung inflammation characterized by a transient influx of neutrophils and eosinophils in the alveolar space. In contrast, a high dose of pristine rGO induced a persistent presence of immune cells in the alveolar space, in particular macrophages associated with the clearance of materials, without affecting the overall resolution of inflammation with time. Importantly, this inflammation in the form of cell recruitment but without cytokine secretion was not associated with any tissue remodelling within the time-frame investigated. Since the administrated bolus dose of 15 μg is considered a high dose, representing a worst-case scenario, the limited animal findings underline the likely low toxicity of the tested abraded composites or the pristine rGO, in any realistic exposure scenario. Overall, the *in vivo* results are in good agreement with the *in vitro* biological assessment data, in particular the lung epithelial cells (A549), the macrophages (THP-1 and RAW 264.7) and neutrophils (HL-60), for which no or limited effects were observed in the tested biological systems upon exposure to PA6-rGO or rGO. At the same time, the *in vivo* results highlight the limitations of single cell type *in vitro* models as alternative models to animals for predictive toxicology and support the current trend to adopt co-culture *in vitro* models to better replicate *in vivo* outcomes. Future studies should therefore investigate the applicability of co-cultures of A549/dTHP-1 cells, lung-on-a-chip, or whole alveoli organoid models for the screening of GRMs.

5. Conclusions

Numerous studies have addressed the hazard potential of GRMs using a variety of model systems (Fadeel et al., 2018). These studies attest to the key importance of defining the properties of the tested materials including the lateral dimensions, thickness, number of layers, and C:O ratio (Wick et al., 2014). It is noted that most, if not all of these studies have been carried out using pristine (as-produced) materials. However, this may not accurately reflect the actual handling and use of GRMs during their life cycle as components of GRM-enabled products (Guineé et al., 2017). In a previous study conducted using multi-walled carbon nanotubes (MWCNTs), the as-produced MWCNTs were shown to elicit inflammation when administered to mice *via* pharyngeal aspiration whereas the aerosols generated from sanding of composites containing polymer-coated MWCNTs, representative of the actual end-product, did not exert such toxicity (Bishop et al., 2017). Herein, we applied similar product life cycle considerations to assess the toxicological impact of rGO in the context of its embedding in a thermoplastic PA6 polymer matrix and its potential release during the life cycle of rGO-reinforced PA6 composites. A multi-endpoint comparison was performed between as-produced rGO, abraded PA6-rGO composite and abraded neat PA6 using a panel of robust and commonly used *in vitro* models as well as a mouse model of pulmonary exposure. Overall, the present findings show a negligible impact of rGO-reinforced PA6 composites on all the models tested, suggesting a likely low risk to human health at acute exposure conditions. Nevertheless, the results found for rGO alone, in particular *in vivo*, suggest that long-term effects after repeated exposure cannot be excluded and further studies are required to address the possible chronic impact of rGO-reinforced composite materials.

Environmental implication statement for the manuscript

'Hazard assessment of abraded thermoplastic composites reinforced with reduced graphene oxide'.

The majority of graphene production is used to reinforce polymers. Despite considerable progress made in recent years in terms of graphene safety assessment, only limited information is available concerning the release and hazard potential of graphene-containing products after mechanical treatment. Airborne particles released into the environment will get into contact with human beings. There are some indications that these released materials might have a hazardous effects in particular after inhalation. With our comprehensive study, we provide clarification on what is released qualitatively and quantitatively and its impact on human health.

Supporting Information

The Supporting Information is available free of charge.

Raman spectra, and FTIR patterns of GO, rGO and functionalised rGO, XPS spectra and TGA analysis of functionalized rGO, representative TEM micrographs of rGO after the APTES functionalization, representative AFM and optical microscopy images of rGO and PA6-rGO, Lateral dimension and thickness distribution analysis for rGO and PA6-rGO, EPR spectra of the powder of PA6, rGO and PA6-rGO and assessment of ROS, particle size distributions of PA6-rGO and PA6 particles measured by SMPS, TNF-α Expression Test (TET) for endotoxin detection in HMDMs exposed to PA6, PA6-rGO, and rGO, representative SEM images of the crack surface of the freeze-fractured samples of neat PA6 and PA6-rGO composite, representative TEM image of the abraded particles from the PA6-rGO composite showing the protruding rGOs from PA6 matrix, IL-6 and IL-8 release after DQ exposure in A549 lung cells, LDH release from RAW 264.7 macrophages after exposure to rGO and abraded PA6 and PA6-rGO for 24 h, IFN-γ, TNF-α and IL-1β release by THP-1 macrophages after incubation with 20 μg/mL of PA6, PA6-rGO and rGO, cell morphology of RAW 264.7 macrophages exposed to different concentrations of rGO and abraded PA6 and PA6-rGO composites, cytokine profiling and hierarchical cluster analysis of inflammatory mediators released in differentiated HL-60 neutrophils exposed to rGO, abraded PA6-rGO and PA6, interference assessment of the abraded particles (PA6 and PA6-rGO) and rGO with the MTS assay.

CRediT authorship contribution statement

Savvina Chortarea: Writing – original draft, Investigation, Formal analysis, Data curation. **Ogul Can Kuru:** investigation. **Woranan Netkueakul:** Methodology, Investigation. **Marco Pelin:** Writing – review & editing, Methodology, Data Curation, Investigation, Validation, Formal analysis, Data Curation. **Sandeep Keshavan:** Methodology, Investigation, Formal analysis, Data Curation. **Zhengmei Song:** Methodology, Investigation. **Baojin Ma:** Methodology, Investigation. **Julio Gómes:** Data curation, Investigation. **Elvira Villaro Abalos:** Data Curation, Investigation. **Luis Augusto Visani de Luna:** Methodology, Investigation. **Thomas Loret:** investigation. **Alexander Fordham:** Investigation. **Matthew Drummond:** investigation. **Nikolaos Kontis:** Methodology, Investigation. **George Anagnostopoulos:** Methodology, Investigation. **George Paterakis:** Methodology, Investigation. **Pietro Cataldi:** Investigation. **Aurelia Tubaro:** Investigation. **Costas Galiotis:** Conceptualization, Supervision, Writing – review & editing, Resources, Data curation, Funding acquisition. **Ian Kinloch:** Data curation, Supervision, Writing – review & editing. **Bengt Fadeel:** Conceptualization, Supervision, Writing – review & editing, validation, resources, project administration, data curation, funding acquisition. **Cyrill Bussy:** Supervision, Writing – review & editing, Validation, Project administration. **Kostas Kostarelos:** Supervision, Writing – review & editing, Resources, Data curation, Funding acquisition. **Tina Buerki-Thurnherr:** Conceptualization, Visualization, Supervision, Validation, Writing – review & editing, Data curation. **Maurizio Prato:** Conceptualization, Supervision, Writing – review & editing, Resources, Project administration, Funding acquisition. **Alberto Bianco:** Conceptualization, Supervision, Writing – review & editing, Resources, Project administration, Funding acquisition. **Peter Wick:** Conceptualization, Supervision, Writing – review & editing, resources, validation, project administration, Funding acquisition.

Declaration of Competing Interest

The authors declare that they have no known competing financial

interests or personal relationships that could have appeared to influence the work reported in this paper.

Acknowledgments

This work was supported by the European Union (EU) 8th Framework Program for Research and Technological Development, Graphene Flagship project (H2020-FET- GrapheneCore2 - #785219 and H2020-FET- GrapheneCore3 - #881603). Part of this work was supported by the University of Trieste, the Agence Nationale de la Recherche (ANR) through the LabEx project Chemistry of Complex Systems (ANR-10-LABX- 0026_CSC), the Maria de Maeztu Units of Excellence Program from the Spanish State Research Agency – Grant No. MDM-2017-0720 and the Swiss National Science Foundation (Grant 310030_169207).

We would like to acknowledge the staff at the Faculty of Biology, Medicine, and Health, the University of Manchester, particularly P. Walker and G.Bako (Histology facility), Dr G. Howell (Flow Cytometry Facility), C. Morrison (Genomic Facility), Dr P. March (Bioimaging Facility), all staff members at the Biological Services Facility for expert advice and assistance in using core facility, and their provision of technical support services. We also wish to acknowledge the Centre National de la Recherche Scientifique (CNRS) and the International Center for Frontier Research in Chemistry (icFRC).

The Bioimaging Facility microscopes used in the *in vivo* part of the study were purchased with grants from the UKRI Biotechnology and Biological Sciences Research Council (UKRI-BBSRC), the Wellcome Trust, and the University of Manchester Strategic Fund.

The graphics for the Table of Contents (ToC) and for Fig. 1 were created using BioRender.com.

Appendix A. Supporting information

Supplementary data associated with this article can be found in the online version at doi:10.1016/j.jhazmat.2022.129053.

References

Accioly, M.T., Pacheco, P., Maya-Monteiro, C.M., Carrossini, N., Robbs, B.K., Oliveira, S. S., Kaufmann, C., Morgado-Diaz, J.A., Bozza, P.T., Viola, J.P.B., 2008. Lipid bodies are reservoirs of cyclooxygenase-2 and sites of prostaglandin-E2 synthesis in colon cancer cells. Cancer Res. 68 (6), 1732–1740. https://doi.org/10.1158/0008-5472.CAN-07-1999.

Ali, G., Mehmood, A., Ha, H.Y., Kim, J., Chung, K.Y., 2017. Reduced graphene oxide as a stable and high-capacity cathode material for na-ion batteries. Sci. Rep. 7 (2), 1–8. https://doi.org/10.1038/srep40910.

Anderson, J.M., Rodriguez, A., Chang, D.T., 2008. Foreign body reaction to biomaterials. Sem. Immun. 86–100. https://doi.org/10.1016/j.smim.2007.11.004.

Barosova, H., Chortarea, S., Peikertova, P., Clift, M.J.D., Petri-Fink, A., Kukutschova, J., Rothen-Rutishauser, B., 2018. Biological response of an in vitro human 3D lung cell model exposed to brake wear debris varies based on brake pad formulation. Arch. Toxicol. 92 (7), 2339–2351. https://doi.org/10.1007/s00204-018-2218-8.

Barosova, H., Maione, A.G., Septiadi, D., Sharma, M., Haeni, L., Balog, S., O'Connell, O., Jackson, G.R., Brown, D., Clippinger, A.J., Hayden, P., Petri-Fink, A., Stone, V., Rothen-Rutishauser, B., 2020. Use of EpiAlveolar lung model to predict fibrotic potential of multiwalled carbon nanotubes. ACS Nano 14 (4), 3941–3956. https://doi.org/10.1021/acsnano.9b06860.

Beams, R., Gustavo Cançado, L., Novotny, L., 2015. Raman characterization of defects and dopants in graphene. J. Phys. Condens. Matter, 083002. https://doi.org/10.1088/0953-8984/27/8/083002.

Bengtson, S., Knudsen, K.B., Kyjovska, Z.O., Berthing, T., Skaug, V., Levin, M., Koponen, I.K., Shivayogimath, A., Booth, T.J., Alonso, B., Pesquera, A., Zurutuza, A., Thomsen, B.L., Troelsen, J.T., Jacobsen, N.R., Vogel, U., 2017. Differences in inflammation and acute phase response but similar genotoxicity in mice following pulmonary exposure to graphene oxide and reduced graphene oxide. PLoS One 12 (6), e0178355. https://doi.org/10.1371/journal.pone.0178355.

Beyeler, S., Chortarea, S., Rothen-Rutishauser, B., Petri-Fink, A., Wick, P., Tschanz, S.A., von Garnier, C., Blank, F., 2018. Acute effects of multi-walled carbon nanotubes on primary bronchial epithelial cells from COPD Patients. Nanotoxicology 12 (7), 699–711. https://doi.org/10.1080/17435390.2018.1472310.

Bhattacharya, K., Kiliç, G., Costa, P.M., Fadeel, B., 2017. Cytotoxicity screening and cytokine profiling of nineteen nanomaterials enables hazard ranking and grouping based on inflammogenic potential. Nanotoxicology 11 (6), 809–826. https://doi.org/10.1080/17435390.2017.1363309.

Bishop, L., Cena, L., Orandle, M., Yanamala, N., Dahm, M.M., Eileen Birch, M., Evans, D. E., Kodali, V.K., Eye, T., Battelli, L., Zeidler-Erdely, P.C., Casuccio, G., Bunker, K., Lupoi, J.S., Lersch, T.L., Stefaniak, A.B., Sager, T., Afshari, A., Schwegler-Berry, D., Friend, S.;, 2017. *In Vivo* toxicity assessment of occupational components of the carbon nanotube life cycle to provide context to potential health effects. In: ACS Nano, 11, pp. 8849–8863. https://doi.org/10.1021/acsnano.7b03038.

Bitounis, D., Parviz, D., Cao, X., Amadei, C.A., Vecitis, C.D., Sunderland, E.M., Thrall, B. D., Fang, M., Strano, M.S., Demokritou, P., 2020. Synthesis and physicochemical transformations of size-sorted graphene oxide during simulated digestion and its toxicological assessment against an *in Vitro* model of the human intestinal epithelium. Small 16 (21), 1907640. https://doi.org/10.1002/smll.201907640.

Blank, F., Rothen-Rutishauser, B.M., Schurch, S., Gehr, P., 2006. An Optimized *in Vitro* model of the respiratory tract wall to study particle cell interactions. J. Aerosol Med. 19 (3), 392–405. https://doi.org/10.1089/jam.2006.19.392.

Böhmert, L., König, L., Sieg, H., Lichtenstein, D., Paul, N., Braeuning, A., Voigt, A., Lampen, A., 2018. *In Vitro* nanoparticle dosimetry for adherent growing cell monolayers covering bottom and lateral walls. Part. Fibre Toxicol. 15 (1), 1–20. https://doi.org/10.1186/S12989-018-0278-9.

Boraschi, D., Italiani, P., Palomba, R., Decuzzi, P., Duschl, A., Fadeel, B., Moghimi, S.M., 2017. Nanoparticles and innate immunity: new perspectives on host defence. Semin. Immun. 33–51. https://doi.org/10.1016/j.smim.2017.08.013.

Bortz, D.R., Heras, E.G., Martin-Gullon, I., 2012. Impressive fatigue life and fracture toughness improvements in graphene oxide/epoxy composites. Macromolecules 45 (1), 238–245. https://doi.org/10.1021/ma201563k.

Carosio, F., Maddalena, L., Gomez, J., Saracco, G., Fina, A., 2018. Graphene oxide exoskeleton to produce self-extinguishing, nonignitable, and flame resistant flexible foams: a mechanically tough alternative to inorganic aerogels. Adv. Mater. Interfaces 5 (23), 1801288. https://doi.org/10.1002/admi.201801288.

Carr, K.E., Smyth, S.H., McCullough, M.T., Morris, J.F., Moyes, S.M., 2012. Morphological aspects of interactions between microparticles and mammalian cells: intestinal uptake and onward movement. Prog. Histochem. Cytochem. 185–252. https://doi.org/10.1016/j.proghi.2011.11.001.

Chang, Y., Yang, S.T., Liu, J.H., Dong, E., Wang, Y., Cao, A., Liu, Y., Wang, H., 2011. *In Vitro* toxicity evaluation of graphene oxide on A549 cells. Toxicol. Lett. 200 (3), 201–210. https://doi.org/10.1016/j.toxlet.2010.11.016.

Chen, G.Y., Yang, H.J., Lu, C.H., Chao, Y.C., Hwang, S.M., Chen, C.L., Lo, K.W., Sung, L. Y., Luo, W.Y., Tuan, H.Y., Hu, Y.C., 2012. Simultaneous induction of autophagy and toll-like receptor signaling pathways by graphene oxide. Biomaterials 33 (27), 6559–6569. https://doi.org/10.1016/j.biomaterials.2012.05.064.

Chortarea, S., Barosova, H., Clift, M.J.D., Wick, P., Petri-Fink, A., Rothen-Rutishauser, B., 2017. Human asthmatic bronchial cells are more susceptible to subchronic repeated exposures of aerosolized carbon nanotubes at occupationally relevant doses than healthy cells. ACS Nano 11 (8), 7615–7625. https://doi.org/10.1021/acsnano.7b01992.

Chortarea, S., Barosova, H., Clift, M.J.D., Wick, P., Petri-Fink, A., Rothen-Rutishauser, B., 2017. Human asthmatic bronchial cells are more susceptible to subchronic repeated exposures of aerosolized carbon nanotubes at occupationally relevant doses than healthy cells. ACS Nano 11 (8), 7615–7625. https://doi.org/10.1021/acsnano.7b01992.

Chortarea, S., Clift, M.J.D., Vanhecke, D., Endes, C., Wick, P., Petri-Fink, A., Rothen-Rutishauser, B., 2015. Repeated exposure to carbon nanotube-based aerosols does not affect the functional properties of a 3D human epithelial airway model. Nanotoxicology 5390, 1–11.

Chortarea, S., Zerimariam, F., Barosova, H., Septiadi, D., Clift, M.J.D., Petri-Fink, A., Rothen-Rutishauser, B., 2019. Profibrotic activity of multiwalled carbon nanotubes upon prolonged exposures in different human lung cell types. Appl. Vitr. Toxicol. 5 (1), 47–61. https://doi.org/10.1089/aivt.2017.0033.

Clouter, A., Brown, D., Höhr, D., Borm, P., Donaldson, K., 2001. Inflammatory effects of respirable quartz collected in workplaces versus standard DQ12 quartz: particle surface correlates. Toxicol. Sci. 63 (1), 90–98.

CY, W., GM, D., A, P., P, D., 2016. Buoyant nanoparticles: implications for nano-biointeractions in cellular studies. Small 12 (23), 3172–3180. https://doi.org/10.1002/SMLL.201600314.

DeLoid, G., Cohen, J.M., Darrah, T., Derk, R., Rojanasakul, L., Pyrgiotakis, G., Wohlleben, W., Demokritou, P., 2014. Estimating the effective density of engineered nanomaterials for in vitro dosimetry. Nat. Commun. 5 (1), 1–10. https://doi.org/10.1038/ncomms4514.

DeLoid, G.M., Cohen, J.M., Pyrgiotakis, G., Pirela, S.V., Pal, A., Liu, J., Srebric, J., Demokritou, P., 2015. Advanced computational modeling for *in Vitro* nanomaterial dosimetry. Part. Fibre Toxicol. 12 (1), 1–20. https://doi.org/10.1186/S12989-015-0109-1.

Dias, F.T.G., Ingracio, A.R., Nicoletti, N.F., Menezes, F.C., Dall Agnol, L., Marinowic, D. R., Soares, R.M.D., da Costa, J.C., Falavigna, A., Bianchi, O., 2019. Soybean-modified polyamide-6 mats as a long-term cutaneous wound covering. Mater. Sci. Eng. C. 99, 957–968. https://doi.org/10.1016/j.msec.2019.02.019.

Domenech, J., Hernández, A., Demir, E., Marcos, R., Cortés, C., 2020. Interactions of graphene oxide and graphene nanoplatelets with the *in Vitro* Caco-2/HT29 model of intestinal barrier. Sci. Rep. 10 (1), 1–15. https://doi.org/10.1038/s41598-020-59755-0.

Drasler, B., Kucki, M., Delhaes, F., Buerki-Thurnherr, T., Vanhecke, D., Korejwo, D., Chortarea, S., Barosova, H., Hirsch, C., Petri-Fink, A., Rothen-Rutishauser, B., Wick, P., 2018. Single exposure to aerosolized graphene oxide and graphene nanoplatelets did not initiate an acute biological response in a 3D human lung model. Carbon N. Y 137, 125–135. https://doi.org/10.1016/J.CARBON.2018.05.012.

Duncan, T.V., Pillai, K., 2015. Release of engineered nanomaterials from polymer nanocomposites: diffusion, dissolution, and desorption. ACS Appl. Mater. Interfaces 2–19. https://doi.org/10.1021/am5062745.

Eckmann, A., Felten, A., Verzhbitskiy, I., Davey, R., Casiraghi, C., 2013. Raman study on defective graphene: effect of the excitation energy, type, and amount of defects. Phys. Rev. B Condens. Matter Mater. Phys. 88 (3), 035426 https://doi.org/10.1103/PhysRevB.88.035426.

EC, C., Q, Z., Y, X., 2011. The effect of sedimentation and diffusion on cellular uptake of gold nanoparticles. Nat. Nanotechnol. 6 (6), 385–391. https://doi.org/10.1038/NNANO.2011.58.

Elliott, J.T., Rösslein, M., Song, N.W., Toman, B., Kinsner-Ovaskainen, A., Maniratanachote, R., Salit, M.L., Petersen, E.J., Sequeira, F., Romsos, E.L., Kim, S.J., Lee, J., Von Moos, N.R., Rossi, F., Hirsch, C., Krug, H.F., Suchaoin, W., Wick, P., 2017. Toward achieving harmonization in a nanocytotoxicity assay measurement through an interlaboratory comparison study. ALTEX 34 (2), 201–218. https://doi.org/10.14573/altex.1605021.

Endes, C., Schmid, O., Kinnear, C., Mueller, S., Camarero-Espinosa, S., Vanhecke, D., Foster, E.J., Petri-Fink, A., Rothen-Rutishauser, B., Weder, C., Clift, M.J., 2014. An *in Vitro* testing strategy towards mimicking the inhalation of high aspect ratio nanoparticles. Part. Fibre Toxicol. 11 (1), 40. https://doi.org/10.1186/s12989-014-0040-x.

Endes, C., Schmid, O., Kinnear, C., Mueller, S., Camarero-Espinosa, S., Vanhecke, D., Foster, E.J., Petri-Fink, A., Rothen-Rutishauser, B., Weder, C., Clift, M.J.D., 2014. An *in Vitro* testing strategy towards mimicking the inhalation of high aspect ratio nanoparticles. Part. Fibre Toxicol. 11 (1) https://doi.org/10.1186/s12989-014-0040-x.

Fadeel, B., Åhlin, A., Henter, J.I., Orrenius, S., Hampton, M.B., 1998. Involvement of caspases in neutrophil apoptosis: regulation by reactive oxygen species. Blood 92 (12), 4808–4818. https://doi.org/10.1182/blood.v92.12.4808.424k01_4808_4818.

Fadeel, B., Bussy, C., Merino, S., Vázquez, E., Flahaut, E., Mouchet, F., Evariste, L., Gauthier, L., Koivisto, A.J., Vogel, U., Martín, C., Delogu, L.G., Buerki-Thurnherr, T., Wick, P., Beloin-Saint-Pierre, D., Hischier, R., Pelin, M., Candotto Carniel, F., Tretiach, M., Cesca, F., 2018. Safety assessment of graphene-based materials: focus on human health and the environment. ACS Nano 10582–10620. https://doi.org/10.1021/acsnano.8b04758.

Farcal, L., Andón, F.T., Di Cristo, L., Rotoli, B.M., Bussolati, O., Bergamaschi, E., Mech, A., Hartmann, N.B., Rasmussen, K., Riego-Sintes, J., Ponti, J., Kinsner-Ovaskainen, A., Rossi, F., Oomen, A., Bos, P., Chen, R., Bai, R., Chen, C., Rocks, L., Fulton, N., 2015. Comprehensive *in Vitro* toxicity testing of a panel of representative oxide nanomaterials: first steps towards an intelligent testing strategy. PLoS One 10 (5). https://doi.org/10.1371/journal.pone.0127174.

Ferrari, A.C., Bonaccorso, F., Fal'ko, V., Novoselov, K.S., Roche, S., Bøggild, P., Borini, S., Koppens, F.H.L., Palermo, V., Pugno, N., Garrido, J.A., Sordan, R., Bianco, A., Ballerini, L., Prato, M., Lidorikis, E., Kivioja, J., Marinelli, C., 2015. Science and technology roadmap for graphene, related two-dimensional crystals, and hybrid systems. Nanoscale 7 (11), 4598–4810. https://doi.org/10.1039/C4NR01600A.

Ferreiro, V., Depecker, C., Laureyns, J., Coulon, G., 2004. Structures and morphologies of cast and plastically strained polyamide 6 films as evidenced by confocal raman microspectroscopy and atomic force microscopy. Polym. (Guildf.) 45 (17), 6013–6026. https://doi.org/10.1016/j.polymer.2004.06.018.

Froggett, S.J., Clancy, S.F., Boverhof, D.R., Canady, R.A., 2014. A review and perspective of existing research on the release of nanomaterials from solid nanocomposites. Part Fibre Toxicol. 1–28. https://doi.org/10.1186/1743-8977-11-17.

Froggett, S.J., Clancy, S.F., Boverhof, D.R., Canady, R.A., 2014. A review and perspective of existing research on the release of nanomaterials from solid nanocomposites. Part. Fibre Toxicol. 1–28. https://doi.org/10.1186/1743-8977-11-17.

Frontiñán-Rubio, J., Victoria Gómez, M., Martín, C., González-Domínguez, J.M., Durán-Prado, M., Vázquez, E., 2018. Differential effects of graphene materials on the metabolism and Function of Human Skin Cells. Nanoscale 10 (24), 11604–11615. https://doi.org/10.1039/c8nr00897c.

Fusco, L., Pelin, M., Mukherjee, S., Keshavan, S., Sosa, S., Martín, C., González, V., Vázquez, E., Prato, M., Fadeel, B., Tubaro, A., 2020. Keratinocytes are capable of selectively sensing low amounts of graphene-based materials: implications for cutaneous applications. Carbon N. Y 159, 598–610. https://doi.org/10.1016/j.carbon.2019.12.064.

Fu, X., Yao, C., Yang, G., 2015. Recent advances in graphene/polyamide 6 composites: a review. RSC Adv. 61688–61702. https://doi.org/10.1039/c5ra09312k.

Gangwal, S., Brown, J.S., Wang, A., Houck, K.A., Dix, D.J., Kavlock, R.J., Cohen Hubal, E. A., 2011. Informing selection of nanomaterial concentrations for toxcast *in vitro* testing based on occupational exposure potential. Environ. Health Perspect. 1539–1546. https://doi.org/10.1289/ehp.1103750.

Geim, A.K., Novoselov, K.S., 2007. The rise of graphene. Nat. Mater. 6 (3), 183–191. https://doi.org/10.1038/nmat1849.

George, G., Sisupal, S.B., Tomy, T., Kumaran, A., Vadivelu, P., Suvekbala, V., Sivaram, S., Ragupathy, L., 2018. Facile, environmentally benign and scalable approach to produce pristine few layers graphene suitable for preparing biocompatible polymer nanocomposites. Sci. Rep. 8 (1), 11228. https://doi.org/10.1038/s41598-018-28560-1.

Golchin, A., Simmons, G., Glavatskih, S., Prakash, B., 2013. Tribological behaviour of polymeric materials in water-lubricated contacts. Proc. Inst. Mech. Eng. Part J. J. Eng. Tribol. 227 (8), 811–825. https://doi.org/10.1177/1350650113476441.

Gomez, J., Villaro, E., Karagiannidis, P.G., Elmarakbi, A., 2020. Effects of chemical structure and morphology of graphene-related materials (GRMs) on melt processing and properties of GRM/Polyamide-6 nanocomposites. Results Mater. 7, 100105 https://doi.org/10.1016/j.rinma.2020.100105.

Gómez, J., Villaro, E., Navas, A., Recio, I., 2017. Testing the influence of the temperature, RH and filler type and content on the universal power law for new reduced graphene oxide TPU composites. Mater. Res. Express 4 (10), 105020. https://doi.org/10.1088/2053-1591/aa8e11.

Gong, L., Yin, B., Li, L.P., Yang, M.B., 2015. Nylon-6/Graphene composites modified through polymeric modification of graphene. Compos. Part B Eng. 73, 49–56. https://doi.org/10.1016/j.compositesb.2014.12.009.

Guarnieri, D., Sánchez-Moreno, P., Del Rio Castillo, A.E., Bonaccorso, F., Gatto, F., Bardi, G., Martín, C., Vázquez, E., Catelani, T., Sabella, S., Pompa, P.P., 2018. Biotransformation and biological interaction of graphene and graphene oxide during simulated oral ingestion. Small 14 (24), 1800227. https://doi.org/10.1002/smll.201800227.

Guineé, J.B., Heijungs, R., Vijver, M.G., Peijnenburg, W.J.G.M., 2017. Setting the stage for debating the roles of risk assessment and life-cycle assessment of engineered nanomaterials. Nat. Nanotech. 727–733. https://doi.org/10.1038/NNANO.2017.135.

Guo, F., Creighton, M., Chen, Y., Hurt, R., Külaots, I., 2014. Porous structures in stacked, crumpled and pillared graphene-based 3D materials. Carbon N. Y 66, 476–484. https://doi.org/10.1016/j.carbon.2013.09.024.

Gurunathan, S., Kang, M.-H., Jeyaraj, M., Kim, J.-H., 2019. Differential Immunomodulatory effect of graphene oxide and vanillin-functionalized graphene oxide nanoparticles in human acute monocytic leukemia cell line (THP-1). Int. J. Mol. Sci. 20 (2), 247. https://doi.org/10.3390/ijms20020247.

Hänel, K.H., Cornelissen, C., Lüscher, B., Baron, J.M., 2013. Cytokines and the skin barrier. Int. J. Mol. Sci. 6720–6745. https://doi.org/10.3390/ijms14046720.

Hansen, G.H., Niels-Christiansen, L.-L., Immerdal, L., Nystrøm, B.T., Danielsen, E.M., 2007. Intestinal alkaline phosphatase: selective endocytosis from the enterocyte brush border during fat absorption. Am. J. Physiol. Liver Physiol. 293 (6), G1325–G1332. https://doi.org/10.1152/ajpgi.00379.2007.

Hempt, C., Hirsch, C., Hannig, Y., Rippl, A., Wick, P., Buerki-Thurnherr, T., 2020. Investigating the effects of differently produced synthetic amorphous silica (E 551) on the integrity and functionality of the human intestinal barrier using an advanced *in Vitro* co-culture model. Arch. Toxicol. 1, 3. https://doi.org/10.1007/s00204-020-02957-2.

Irfan, A., Sachse, S., Njuguna, J., Pielichowski, K., Silva, F., Zhu, H., 2013. Assessment of nanoparticle release from polyamide 6- and polypropylene-silicon composites and cytotoxicity in human lung A549 cells. J. Inorg. Organomet. Polym. Mater. 23 (4), 861–870. https://doi.org/10.1007/s10904-013-9856-3.

Jian, L., Ning, L., Yang, S., Wang, J., Hua, M., 2009. Triboelectrification electrostatic potential of MC Nylon 6 under point contact dry sliding. Tribol. Lett. 36 (3), 199–208. https://doi.org/10.1007/s11249-009-9473-z.

Keshavan, S., Calligari, P., Stella, L., Fusco, L., Delogu, L.G., Fadeel, B., 2019. Nano-bio interactions: a neutrophil-centric view. Cell Death Dis. 1–11. https://doi.org/10.1038/s41419-019-1806-8.

Khandagale, A., Lazzaretto, B., Carlsson, G., Sundin, M., Shafeeq, S., Römling, U., Fadeel, B., 2018. JAGN1 Is required for fungal killing in neutrophil extracellular traps: implications for severe congenital neutropenia. J. Leukoc. Biol. 1–15. https://doi.org/10.1002/JLB.4A0118-030RR.

Kong, W., Kum, H., Bae, S.H., Shim, J., Kim, H., Kong, L., Meng, Y., Wang, K., Kim, C., Kim, J., 2019. Path towards graphene commercialization from lab to market. Nat. Nanotechnol. 927–938. https://doi.org/10.1038/s41565-019-0555-2.

Krishnamoorthy, K., Veerapandian, M., Mohan, R., Kim, S.J., 2012. Investigation of Raman and photoluminescence studies of reduced graphene oxide sheets. Appl. Phys. A Mater. Sci. Process. 106 (3), 501–506. https://doi.org/10.1007/s00339-011-6720-6.

Krysiak, Z.J., Gawlik, M.Z., Knapczyk-Korczak, J., Kaniuk, L., Stachewicz, U., 2020. Hierarchical composite meshes of electrospun PS microfibers with PA6 nanofibers for regenerative medicine. Materials 13 (8), 1974. https://doi.org/10.3390/MA13081974.

Kucki, M., Aengenheister, L., Diener, L., Rippl, A.V., Vranic, S., Newman, L., Vazquez, E., Kostarelos, K., Wick, P., Buerki-Thurnherr, T., 2018. Impact of Graphene Oxide on Human Placental Trophoblast Viability, Functionality and Barrier Integrity. 2D Mater. 5 (3), 035014 https://doi.org/10.1088/2053–1583/aab9e2.

Kucki, M., Diener, L., Bohmer, N., Hirsch, C., Krug, H.F., Palermo, V., Wick, P., 2017. Uptake of label-free graphene oxide by caco-2 cells is dependent on the cell differentiation status. J. Nanobiotechnol. 15 (1), 46. https://doi.org/10.1186/s12951-017-0280-7.

Kucki, M., Rupper, P., Sarrieu, C., Melucci, M., Treossi, E., Schwarz, A., León, V., Kraegeloh, A., Flahaut, E., Vázquez, E., Palermo, V., Wick, P., 2016. Interaction of graphene-related materials with human intestinal cells: an *in Vitro* approach. Nanoscale 8 (16), 8749–8760. https://doi.org/10.1039/c6nr00319b.

Kurapati, R., Russier, J., Squillaci, M.A., Treossi, E., Ménard-Moyon, C., Del Rio-Castillo, A.E., Vazquez, E., Samorì, P., Palermo, V., Bianco, A., 2015. Dispersibility-dependent biodegradation of graphene oxide by myeloperoxidase. Small 11 (32), 3985–3994. https://doi.org/10.1002/smll.201500038.

Lankone, R.S., Ruggiero, E., Goodwin, D.G., Vilsmeier, K., Mueller, P., Pulbere, S., Challis, K., Bi, Y., Westerhoff, P., Ranville, J., Fairbrother, D.H., Sung, L.-P., Wohlleben, W., 2020. Evaluating performance, degradation, and release behavior of a nanoform pigmented coating after natural and accelerated weathering. NanoImpact 17.

Lin, H., Song, Z., Bianco, A., 2021. How macrophages respond to two-dimensional materials: a critical overview focusing on toxicity. J. Environ. Sci. Health 333–356. https://doi.org/10.1080/03601234.2021.1885262.

Liu, Y., Luo, Y., Wu, J., Wang, Y., Yang, X., Yang, R., Wang, B., Yang, J., Zhang, N., 2013. Graphene oxide can induce *in Vitro* and *in Vivo* mutagenesis. Sci. Rep. 3. https://doi.org/10.1038/srep03469.

Li, Y., Boraschi, D., 2016. Endotoxin contamination: a key element in the interpretation of nanosafety studies. Nanomedicine 269–287. https://doi.org/10.2217/nnm.15.196.

Li, R., Guiney, L.M., Chang, C.H., Mansukhani, N.D., Ji, Z., Wang, X., Liao, Y.P., Jiang, W., Sun, B., Hersam, M.C., Nel, A.E., Xia, T., 2018. Surface oxidation of graphene oxide determines membrane damage, lipid peroxidation, and cytotoxicity in macrophages in a pulmonary toxicity model. ACS Nano 12 (2), 1390–1402. https://doi.org/10.1021/acsnano.7b07737.

Li, J., Wang, X., Mei, K.C., Chang, C.H., Jiang, J., Liu, X., Liu, Q., Guiney, L.M., Hersam, M.C., Liao, Y.P., Meng, H., Xia, T., 2021. Lateral size of graphene oxide determines differential cellular uptake and cell death pathways in kupffer cells, LSECs, and hepatocytes. Nano Today 37, 101061. https://doi.org/10.1016/J.NANTOD.2020.101061.

Li, B., Yang, J., Huang, Q., Zhang, Y., Peng, C., Zhang, Y., He, Y., Shi, J., Li, W., Hu, J., Fan, C., 2013. Biodistribution and pulmonary toxicity of intratracheally instilled graphene oxide in mice. NPG Asia Mater. 5 (4) https://doi.org/10.1038/am.2013.7.

Massaq, A., Rusinek, A., Klosak, M., Bahi, S., Arias, A., 2019. Strain rate effect on the mechanical behavior of polyamide composites under compression loading. Compos. Struct. 214, 114–122. https://doi.org/10.1016/j.compstruct.2019.01.101.

Ma, J., Liu, R., Wang, X., Liu, Q., Chen, Y., Valle, R.P., Zuo, Y.Y., Xia, T., Liu, S., 2015. Crucial role of lateral size for graphene oxide in activating macrophages and stimulating pro-inflammatory responses in cells and animals. ACS Nano 9 (10), 10498–10515. https://doi.org/10.1021/acsnano.5b04751.

Mercer, R.R., Scabilloni, J.F., Hubbs, A.F., Wang, L., Battelli, L.A., McKinney, W., Castranova, V., Porter, D.W., 2013. Extrapulmonary transport of MWCNT following inhalation exposure. Part. Fibre Toxicol. 10 (1), 38. https://doi.org/10.1186/1743-8977-10-38.

Mittal, S., Kumar, V., Dhiman, N., Chauhan, L.K.S., Pasricha, R., Pandey, A.K., 2016. Physico-chemical properties based differential toxicity of graphene oxide/reduced graphene oxide in human lung cells mediated through oxidative stress. Sci. Rep. 6 (1), 1–16. https://doi.org/10.1038/srep39548.

Moalli, P.A., MacDonald, J.L., Goodglick, L.A., Kane, A.B., 1987. Acute injury and regeneration of the mesothelium in response to asbestos fibers. Am. J. Pathol. 128 (3), 426–445.

Monteiller, C., Tran, L., MacNee, W., Faux, S., Jones, A., Miller, B., Donaldson, K., 2007. The Pro-inflammatory effects of low-toxicity low-solubility particles, nanoparticles and fine particles, on epithelial cells *in Vitro*: the role of surface area. Occup. Environ. Med. 64 (9), 609–615. https://doi.org/10.1136/oem.2005.024802.

Mouhmid, B., Imad, A., Benseddiq, N., Benmedakhène, S., Maazouz, A., 2006. A Study of the mechanical behaviour of a glass fibre reinforced polyamide 6,6: experimental investigation. Polym. Test. 25 (4), 544–552. https://doi.org/10.1016/j.polymertesting.2006.03.008.

Mukaida, N., 2003. Pathophysiological roles of interleukin-8/CXCL8 in pulmonary diseases. Am. J. Physiol. Lung Cell. Mol. Physiol. https://doi.org/10.1152/ajplung.00233.2002.

Mukherjee, S.P., Bottini, M., Fadeel, B., 2017. Graphene and the immune system: a romance of many dimensions. Fro. Immun. 1. https://doi.org/10.3389/fimmu.2017.00673.

Mukherjee, S.P., Gliga, A.R., Lazzaretto, B., Brandner, B., Fielden, M., Vogt, C., Newman, L., Rodrigues, A.F., Shao, W., Fournier, P.M., Toprak, M.S., Star, A., Kostarelos, K., Bhattacharya, K., Fadeel, B., 2018. Graphene oxide is degraded by neutrophils and the degradation products are non-genotoxic. Nanoscale 10 (3), 1180–1188. https://doi.org/10.1039/c7nr03552g.

Mukherjee, S.P., Kostarelos, K., Fadeel, B., 2018. Cytokine profiling of primary human macrophages exposed to endotoxin-free graphene oxide: size-independent NLRP3 inflammasome activation. Adv. Healthc. Mater. 7 (4), 1700815 https://doi.org/10.1002/adhm.201700815.

Mukherjee, S.P., Lazzaretto, B., Hultenby, K., Newman, L., Rodrigues, A.F., Lozano, N., Kostarelos, K., Malmberg, P., Fadeel, B., 2018. Graphene oxide elicits membrane lipid changes and neutrophil extracellular trap formation. Chem 4 (2), 334–358. https://doi.org/10.1016/j.chempr.2017.12.017.

Mukherjee, S.P., Lozano, N., Kucki, M., Del Rio-Castillo, A.E., Newman, L., Vázquez, E., Kostarelos, K., Wick, P., Fadeel, B., 2016. Detection of endotoxin contamination of graphene based materials using the TNF-α expression test and guidelines for endotoxin-free graphene Oxide production. PLoS One 11 (11), e0166816. https://doi.org/10.1371/journal.pone.0166816.

Nakano-Narusawa, Y., Yokohira, M., Yamakawa, K., Saoo, K., Imaida, K., Matsuda, Y., 2020. Single intratracheal quartz instillation induced chronic inflammation and tumourigenesis in rat lungs. Sci. Rep. 10 (1), 1–10. https://doi.org/10.1038/s41598-020-63667-4.

Nel, A., Xia, T., Mädler, L., Li, N., 2006. Toxic potential of materials at the nanolevel. Science 311 (5761), 622–627. https://doi.org/10.1126/science.1114397.

Netkueakul, W., Fischer, B., Walder, C., Nüesch, F., Rees, M., Jovic, M., Gaan, S., Jacob, P., Wang, J., 2020. Effects of combining graphene nanoplatelet and phosphorous flame retardant as additives on mechanical properties and flame retardancy of epoxy nanocomposite. Polym. (Basel) 12 (10), 2349. https://doi.org/10.3390/polym12102349.

Netkueakul, W., Korejwo, D., Hammer, T., Chortarea, S., Rupper, P., Braun, O., Calame, M., Rothen-Rutishauser, B., Buerki-Thurnherr, T., Wick, P., Wang, J., 2020. Release of graphene-related materials from epoxy-based composites: characterization, quantification and hazard assessment: *in Vitro*. Nanoscale 12 (19), 10703–10722. https://doi.org/10.1039/c9nr10245k.

Novoselov, K.S., Fal'Ko, V.I., Colombo, L., Gellert, P.R., Schwab, M.G., Kim, K., 2012. A roadmap for graphene. Nature 192–200. https://doi.org/10.1038/nature11458.

Oberdörster, G., Oberdörster, E., Oberdörster, J., 2005. Nanotoxicology: an emerging discipline evolving from studies of ultrafine particles. Environ. Health Perspect. 113 (7), 823–839. https://doi.org/10.1289/ehp.7339.

Oberdörster, G., Stone, V., Donaldson, K., 2009. Toxicology of nanoparticles: a historical perspective. Nanotoxicology.

Ou, L., Song, B., Liang, H., Liu, J., Feng, X., Deng, B., Sun, T., Shao, L., 2016. Toxicity of graphene-family nanoparticles: a general review of the origins and mechanisms. Part Fibre Toxicol. 1–24. https://doi.org/10.1186/s12989-016-0168-y.

O'Neill, A., Bakirtzis, D., Dixon, D., 2014. Polyamide 6/graphene composites: the effect of in situ polymerisation on the structure and properties of graphene oxide and reduced graphene oxide. Eur. Polym. J. 59, 353–362. https://doi.org/10.1016/j.eurpolymj.2014.07.038.

Pant, H.R., Pant, B., Park, C.H., Kim, H.J., Lee, D.S., Tijing, L.D., Hwang, B.S., Kim, H.Y., Kim, C.S., 2013. RGO/Nylon-6 composite mat with unique structural features and electrical properties obtained from electrospinning and hydrothermal process. Fibers Polym. 14 (6), 970–975. https://doi.org/10.1007/s12221-013-0970-1.

Pelin, M., Fusco, L., León, V., Martín, C., Criado, A., Sosa, S., Vázquez, E., Tubaro, A., Prato, M., 2017. Differential cytotoxic effects of graphene and graphene oxide on skin keratinocytes. Sci. Rep. 7 https://doi.org/10.1038/srep40572.

Pelin, M., Fusco, L., Martín, C., Sosa, S., Frontiñán-Rubio, J., González-Domínguez, J.M., Durán-Prado, M., Vázquez, E., Prato, M., Tubaro, A., 2018. Graphene and graphene oxide induce ROS production in human HaCaT skin keratinocytes: the role of xanthine oxidase and NADH dehydrogenase. Nanoscale 10 (25), 11820–11830. https://doi.org/10.1039/c8nr02933d.

Pelin, M., Lin, H., Gazzi, A., Sosa, S., Ponti, C., Ortega, A., Zurutuza, A., Vázquez, E., Prato, M., Tubaro, A., Bianco, A., 2020. Partial reversibility of the cytotoxic effect induced by graphene-based materials in skin keratinocytes. Nanomaterials 10 (8), 1–14. https://doi.org/10.3390/nano10081602.

Pelin, M., Sosa, S., Prato, M., Tubaro, A., 2018. Occupational exposure to graphene based nanomaterials: risk assessment. Nanoscale 15894–15903. https://doi.org/10.1039/c8nr04950e.

Pietroiusti, A., Bergamaschi, E., Campagna, M., Campagnolo, L., De Palma, G., Iavicoli, S., Leso, V., Magrini, A., Miragoli, M., Pedata, P., Palombi, L., Iavicoli, I., 2017. The unrecognized occupational relevance of the interaction between engineered nanomaterials and the gastro-intestinal tract: a consensus paper from a multidisciplinary working group. Part. Fibre Toxicol. https://doi.org/10.1186/s12989-017-0226-0.

Poulsen, S.S., Bengtson, S., Williams, A., Jacobsen, N.R., Troelsen, J.T., Halappanavar, S., Vogel, U., 2021. A transcriptomic overview of lung and liver changes one day after pulmonary exposure to graphene and graphene oxide. Toxicol. Appl. Pharmacol. 410, 115343 https://doi.org/10.1016/j.taap.2020.115343.

Reiss, T., Hjelt, K., Ferrari, A.C., 2019. Graphene is on track to deliver on its promises. Nat. Nanotech. 907–910. https://doi.org/10.1038/s41565-019-0557-0.

Reshma, S.C., Syama, S., Mohanan, P.V., 2016. Nano-biointeractions of PEGylated and bare reduced graphene oxide on lung alveolar epithelial cells: a comparative *in Vitro* study. Colloids Surf. B Biointerfaces 140, 104–116. https://doi.org/10.1016/j.colsurfb.2015.12.030.

Rincon, M., Irvin, C.G., 2012. Role of IL-6 in asthma and other inflammatory pulmonary diseases. Intern. J. Biol. Sci. 1281–1290. https://doi.org/10.7150/ijbs.4874.

Roberts, J.R., Mercer, R.R., Stefaniak, A.B., Seehra, M.S., Geddam, U.K., Chaudhuri, I.S., Kyrlidis, A., Kodali, V.K., Sager, T., Kenyon, A., Bilgesu, S.A., Eye, T., Scabilloni, J.F., Leonard, S.S., Fix, N.R., Schwegler-Berry, D., Farris, B.Y., Wolfarth, M.G., Porter, D. W., Castranova, V., 2016. Evaluation of pulmonary and systemic toxicity following lung exposure to graphite nanoplates: a member of the graphene-based nanomaterial family. Part. Fibre Toxicol. 13 (1), 1–22. https://doi.org/10.1186/s12989-016-0145-5.

Rodrigues, A.F., Newman, L., Jasim, D., Mukherjee, S.P., Wang, J., Vacchi, I.A., Ménard-Moyon, C., Bianco, A., Fadeel, B., Kostarelos, K., Bussy, C., 2020. Size-dependent pulmonary impact of thin graphene oxide sheets in mice: toward safe-by-design. Adv. Sci. 7 (12), 1903200 https://doi.org/10.1002/advs.201903200.

Russier, J., Treossi, E., Scarsi, A., Perrozzi, F., Dumortier, H., Ottaviano, L., Meneghetti, M., Palermo, V., Bianco, A., 2013. Evidencing the mask effect of graphene oxide: a comparative study on primary human and murine phagocytic cells. Nanoscale 5 (22), 11234–11247. https://doi.org/10.1039/c3nr03543c.

Schinwald, A., Murphy, F.A., Jones, A., MacNee, W., Donaldson, K., 2012. Graphene-based nanoplatelets: a new risk to the respiratory system as a consequence of their unusual aerodynamic properties. ACS Nano 6 (1), 736–746. https://doi.org/10.1021/nn204229f.

Schlagenhauf, L., Buerki-Thurnherr, T., Kuo, Y.Y., Wichser, A., Nüesch, F., Wick, P., Wang, J., 2015. Carbon nanotubes released from an epoxy-based nanocomposite: quantification and particle toxicity. Environ. Sci. Technol. 49 (17), 10616–10623. https://doi.org/10.1021/acs.est.5b02750.

Shi, Y., Yu, B., Zheng, Y., Yang, J., Duan, Z., Hu, Y., 2018. Design of reduced graphene oxide decorated with DOPO-phosphanomidate for enhanced fire safety of epoxy resin. J. Colloid Interface Sci. 521, 160–171. https://doi.org/10.1016/j.jcis.2018.02.054.

Skehan, P., Storeng, R., Scudiero, D., Monks, A., Mcmahon, J., Vistica, D., Warren, J.T., Bokesch, H., Kenney, S., Boyd, M.R., 1990. New colorimetric cytotoxicity assay for anticancer-drug screening. J. Natl. Cancer Inst. 82 (13), 1107–1112. https://doi.org/10.1093/jnci/82.13.1107.

Sohal, I.S., O'Fallon, K.S., Gaines, P., Demokritou, P., Bello, D., 2018. Ingested engineered nanomaterials: state of science in nanotoxicity testing and future research needs. Part. Fibre Toxicol. 1–31. https://doi.org/10.1186/s12989-018-0265-1.

Song, P., Cao, Z., Cai, Y., Zhao, L., Fang, Z., Fu, S., 2011. Fabrication of exfoliated graphene-based polypropylene nanocomposites with enhanced mechanical and thermal properties. Polym. (Guildf.) 52 (18), 4001–4010. https://doi.org/10.1016/j.polymer.2011.06.045.

Song, Z.M., Chen, N., Liu, J.H., Tang, H., Deng, X., Xi, W.S., Han, K., Cao, A., Liu, Y., Wang, H., 2015. Biological effect of food additive titanium dioxide nanoparticles on

intestine: an *in Vitro* study. J. Appl. Toxicol. 35 (10), 1169–1178. https://doi.org/10.1002/jat.3171.

Song, N., Yang, J., Ding, P., Tang, S., Shi, L., 2015. Effect of polymer modifier chain length on thermal conductive property of polyamide 6/graphene nanocomposites. Compos. Part A Appl. Sci. Manuf. 73, 232–241. https://doi.org/10.1016/j.compositesa.2015.03.018.

Stankovich, S., Dikin, D.A., Dommett, G.H.B., Kohlhaas, K.M., Zimney, E.J., Stach, E.A., Piner, R.D., Nguyen, S.B.T., Ruoff, R.S., 2006. Graphene-based composite materials. Nature 442 (7100), 282–286. https://doi.org/10.1038/nature04969.

Sun, B., Wang, X., Ji, Z., Li, R., Xia, T., 2013. NLRP3 inflammasome activation induced by engineered nanomaterials. Small 1595–1607. https://doi.org/10.1002/smll.201201962.

Su, W.C., Ku, B.K., Kulkarni, P., Cheng, Y.S., 2016. Deposition of graphene nanomaterial aerosols in human upper airways. J. Occup. Environ. Hyg. 13 (1), 48–59. https://doi.org/10.1080/15459624.2015.1076162.

Wang, X., Duch, M.C., Mansukhani, N., Ji, Z., Liao, Y.-P., Wang, M., Zhang, H., Sun, B., Chang, C.H., Li, R., Lin, S., Meng, H., Xia, T., Hersam, M.C., Nel, A.E., 2015. Use of a pro-fibrogenic mechanism-based predictive toxicological approach for tiered testing and decision analysis of carbonaceous nanomaterials. ACS Nano 9 (3), 3032–3043. https://doi.org/10.1021/nn507243w.

Wang, Y., Wu, S., Zhao, X., Su, Z., Du, L., Sui, A., 2014. In vitro toxicity evaluation of graphene oxide on human RPMI 8226 Cells. In: Bio-Medical Materials and Engineering, Vol. 24. IOS Press,, pp. 2007–2013. https://doi.org/10.3233/BME-141010.

Wang, Y., Yu, J., Dai, W., Song, Y., Wang, D., Zeng, L., Jiang, N., 2015. Enhanced thermal and electrical properties of epoxy composites reinforced with graphene nanoplatelets. Polym. Compos. 36 (3), 556–565. https://doi.org/10.1002/pc.22972.

Wan, Y.J., Gong, L.X., Tang, L.C., Wu, L., Bin, Jiang, J.X., 2014. Mechanical properties of epoxy composites filled with silane-functionalized graphene oxide. Compos. Part A Appl. Sci. Manuf. 64, 79–89. https://doi.org/10.1016/j.compositesa.2014.04.023.

Waquier, L., Myles, B.S., Henrard, L., Vautard, F., Pappas, C.M., Feneon, B., Delaitre, C., Mehlem, J.J., Khripin, C.Y., 2020. Quantitative measurement of nanoparticle release from rubber composites during fabrication and testing. J. Nanopart. Res. 22 (9), 1–10. https://doi.org/10.1007/S11051-020-04977-6/FIGURES/5.

Wick, P., Louw-Gaume, A.E., Kucki, M., Krug, H.F., Kostarelos, K., Fadeel, B., Dawson, K. A., Salvati, A., Vázquez, E., Ballerini, L., Tretiach, M., Benfenati, F., Flahaut, E., Gauthier, L., Prato, M., Bianco, A., 2014. Classification framework for graphene-based materials. Angew. Chem. Int. Ed. 53 (30), 7714–7718. https://doi.org/10.1002/anie.201403335.

Wilbourn, J.D., McGregor, D.B., Partensky, C., Rice, J.M., 1997. IARC reevaluates silica and related substances. Environ. Health Perspect. 105 (7), 756–759. https://doi.org/10.1289/ehp.97105756.

Williams, G.T., Williams, W.J., 1983. Granulomatous inflammation - a review. J. Clin. Pathol. 723–733. https://doi.org/10.1136/jcp.36.7.723.

Wohlleben, W., Meier, M.W., Vogel, S., Landsiedel, R., Cox, G., Hirth, S., Tomović, Ž., 2013. Elastic CNT-polyurethane nanocomposite: synthesis, performance and assessment of fragments released during use. Nanoscale 5 (1), 369–380. https://doi.org/10.1039/c2nr32711b.

Wu, J., Wang, Y., Liu, G., Jia, Y., Yang, J., Shi, J., Dong, J., Wei, J., Liu, X., 2018. Characterization of air-liquid interface culture of A549 alveolar epithelial cells. Braz. J. Med. Biol. Res. 51 (2) https://doi.org/10.1590/1414-431x20176950.

Wu, Y., Wang, F., Wang, S., Ma, J., Xu, M., Gao, M., Liu, R., Chen, W., Liu, S., 2018. Reduction of graphene oxide alters its cyto-compatibility towards primary and immortalized macrophages. Nanoscale 10 (30), 14637–14650. https://doi.org/10.1039/c8nr02798f.

Xu, Z., Gao, C., 2010. *In Situ* polymerization approach to graphene-reinforced nylon-6 composites. Macromolecules 43 (16), 6716–6723. https://doi.org/10.1021/ma1009337.

Zaman, I., Kuan, H.C., Dai, J., Kawashima, N., Michelmore, A., Sovi, A., Dong, S., Luong, L., Ma, J., 2012. From carbon nanotubes and silicate layers to graphene platelets for polymer nanocomposites. Nanoscale 4 (15), 4578–4586. https://doi.org/10.1039/c2nr30837a.

Zeng, C., Lu, S., Xiao, X., Gao, J., Pan, L., He, Z., Yu, J., 2015. Enhanced thermal and mechanical properties of epoxy composites by mixing noncovalently functionalized graphene sheets. Polym. Bull. 72 (3), 453–472. https://doi.org/10.1007/s00289-014-1280-5.

Zepp, R., Ruggiero, E., Acrey, B., Acrey, B., Davis, M.J.B., Davis, M.J.B., Han, C., Han, C., Han, C., Hsieh, H.S., Hsieh, H.S., Vilsmeier, K., Wohlleben, W., Sahle-Demessie, E., 2020. Fragmentation of polymer nanocomposites: modulation by dry and wet weathering, fractionation, and nanomaterial filler. Environ. Sci. Nano 7 (6), 1742–1758. https://doi.org/10.1039/c9en01360a.

Zhang, Y., Bai, Y., Jia, J., Gao, N., Li, Y., Zhang, R., Jiang, G., Yan, B., 2014. Perturbation of physiological systems by nanoparticles. Chem. Soc. Rev. 3762–3809. https://doi.org/10.1039/c3cs60338e.

Zhao, X., Zhang, Q., Chen, D., Lu, P., 2010. Enhanced mechanical properties of graphene-based polyvinyl alcohol composites. Macromolecules 43 (5), 2357–2363. https://doi.org/10.1021/ma902862u.

Zheng, W., Chen, W.G., zhao, Q., Ren, S.X., Fu, Y.Q., 2019. Interfacial structures and mechanisms for strengthening and enhanced conductivity of graphene/epoxy nanocomposites. Polymer 163, 171–177. https://doi.org/10.1016/j.polymer.2018.12.055.

Zhou, H., Zhao, K., Li, W., Yang, N., Liu, Y., Chen, C., Wei, T., 2012. The interactions between pristine graphene and macrophages and the production of cytokines/chemokines *via* TLR- and NF-KB-related signaling pathways. Biomaterials 33 (29), 6933–6942. https://doi.org/10.1016/j.biomaterials.2012.06.064.

Zok, F.W., Miserez, A., 2007. Property maps for abrasion resistance of materials. Acta Mater. 55 (18), 6365–6371. https://doi.org/10.1016/j.actamat.2007.07.042.